Predicting hydrogen microporosity in long solidification range ternary Al-Cu-Li alloys by coupling CALPHAD and cellular automata model

Xingxing Li[a], Xinghai Yang[a], Chengpeng Xue[a], Shuo Wang[a], Yuxuan Zhang[a], Bing Wang[a], Junsheng Wang [a,b,*], Peter D. Lee[c,d]

[a] School of Materials Science and Engineering, Beijing Institute of Technology, Beijing, 100081, China

[b] Advanced Research Institute of Multidisciplinary Science, Beijing Institute of Technology, Beijing, 100081, China

[c] Department of Mechanical Engineering, University College London, WC1E 7JE, UK

[d] Research Complex at Harwell, Rutherford Appleton Laboratory, Harwell, Didcot, OX11 0FA, UK

* Corresponding author. Tel.: +86 010 68915043. E-mail: junsheng.wang@bit.edu.cn (J.S. Wang).

Abstract

Aluminum-lithium alloys have wide applications in aerospace industries in the 21st century but their manufacturing is extremely difficult due to the 10 times more equilibrium hydrogen concentration in the liquid than the solubility limit in traditional Al alloys (0.036 ml/100gSTP). The reduction of solubility from liquid to solid by 95% leads to hydrogen porosity being hard to control. In this work, a three-dimensional multicomponent cellular automaton (CA) model is coupled with CALPHAD calculations to simulate the nucleation and growth of hydrogen porosity and its interaction with surrounding dendritic structures during the solidification of Al-Cu-Li alloys. By quantifying the effects of hydrogen concentration, cooling rate, and Li content, it was found the solidification conditions can effectively reduce porosity size. To validate the model, X-ray computed tomography (XCT) has been used to obtain not only the size but also the morphology of porosity as a function of cooling conditions. It was found that porosity grows elongated and tortuous shape at slow cooling rates between columnar dendrites, filling up the empty spaces of secondary arms, while it tends to be dispersed spherical shape when its surrounding grains are refined to equiaxed structures at high cooling rates.

Keywords: Solidification; Al-Cu-Li alloys; Microporosity; Cellular automaton; X-ray CT

1 Introduction

As one of the lightweight, high strength and modulus, and corrosion-resistant materials, aluminum-lithium alloy is increasingly used in aerospace fields, including lunar/deep space exploration spacecraft [1-5]. However, the manufacturing of high-quality Al-Cu-Li alloys is very difficult. This is because the solubility of hydrogen in the liquid is 2.5~3.5 times that of traditional aluminum alloys [6]. The excess amount of hydrogen in the liquid has to be released into the ambient or form porosity because the solubility of hydrogen in the solid is only 5% of the liquid as experimentally measured previously [7]. pore sizes over 100 μm are the crack initiators for fatigue cracks and reduce the ductility of structural components significantly as reported by Yi and Lee [8]. Therefore, hydrogen porosity defect has become the limiting factor for its application in critical structural components [9, 10].

To control the pore size, the growth kinetics of hydrogen porosities in the third generation of Al-Cu-Li alloys have to be quantified. In the early 1990s, Lee and Hunt [11] used X-ray radiography to observe and quantify the effects of different Cu contents, initial H concentrations, and temperature gradients(G) on the nucleation and growth of hydrogen porosity during the directional solidification of Al-Cu alloys. It was found that for a certain concentration of Cu (10wt.%), the supersaturation before nucleation increased from 0.26 to 1.01 and the maximum pore size increased nearly 3.2 times when the hydrogen concentration in the liquid increased from 0.07 mL/100g to 0.27 mL/100g. Lee and Wang [12] performed the *in situ* observation of the kinetics of hydrogen porosity nucleation and growth in Al-4 wt.%Cu and Al-12 wt.%Cu and found that hydrogen diffusion was the dominating mechanism. By taking into account the effect of Cu on the solubility of hydrogen in the aluminum liquids, they have calculated that the pore size increased as a function of Cu additions. In addition, the dendrites in Al-4 wt.%Cu are narrowly spaced and the secondary dendrite arms restrict the liquid flow, causing the hydrogen porosities to expand abruptly downward and fill the solidification shrinkage in their *in situ* observation. Felberbaum and Rappaz [13] used high-precision X-ray tomography to observe microscopic porosity in Al-Cu alloys and to estimate the curvature of the hydrogen porosities, establishing the correlation between neighboring hydrogen porosities from two-dimensional metallography and three-dimensional connected monolithic hydrogen porosities in XCT. Recently, Xue *et al.* [5] found hydrogen porosity accumulation along the welding line in Wire Arc Additive Manufacturing (WAAM) of Al-Cu-Li alloys, which reduces the as-deposited and T6 mechanical properties significantly. Therefore, they proposed a new process to close the hydrogen porosities by different levels of hot deformation and successfully found that the 42% hot deformation was enough to reduce pore size from 100 μm to 30 μm, increasing the UTS and elongation from 264 MPa to 439 MPa and 7.0%, respectively. The mechanism of hydrogen porosity healing was identified to be the compression stress around the hydrogen porosities using finite element analysis.

By fitting the nucleation kinetics of hydrogen porosity in Al-Cu alloys from *in situ* observations, many authors have developed stochastic models for hydrogen porosity nucleation and hydrogen diffusion-controlled growth. Lee *et al.* [14, 15] developed a microscopic hydrogen porosity nucleation model based on the Gaussian function from *in situ* observation of porosity nucleation in Al-Cu and Al-Si alloys. The nuclei size is a function of local hydrogen supersaturation in the liquid. Following this path, Wang and Lee [16, 17] developed a multicomponent pore model based on *in situ* observation of hydrogen porosity nucleation and growth using synchrotron x-ray radiography and tomography. They found that the Fe-rich intermetallics have a large impact on the pore size [17]. Due to the failure of the shrinkage porosity model in predicting hydrogen porosity nucleation and growth in reality, Rappaz *et al.* [18] coupled the FEM model with a hydrogen diffusion-controlled model to predict the pore size distribution in ProCast and implemented it as a subroutine. Similar to ProCast, another leading casting software, Magmasoft, has also taken into account hydrogen diffusion which was implemented by Carlson and Beckermann [19-24]. Recently, Zhu *et al.* [25] created *in situ* observation equipment and started to quantify the porosity nucleation in Al-Si alloys and use the kinetic data in their CA model for predicting the evolution of hydrogen porosity. Zhang *et al.* [26] also developed a porosity model in Al-Cu alloys but they considered the hydrogen porosities as a solid body that does not shrink as hydrogen depletes.

Since Li is very reactive and hard to control, there is no current *in situ* observation or model development for hydrogen porosity in Al-Cu-Li alloys. In this research, we made the first attempt to predict the hydrogen porosity in the third-generation Al-Cu-Li alloys. Based on the Al-Cu and Al-Si-Cu models developed by Lee and Wang *et al.* [16, 27, 28]. we modified the model by considering the effect of Li, including the hydrogen solubility of Al-Cu-Li alloy, the equilibrium partitioning, and diffusion of the Li. The nucleation and growth of primary Al, the evolution of porosity, the distribution of alloy solute and dissolved hydrogen, and the interaction between porosity and primary Al during the solidification of Al-4.8 wt%Cu-1.8 wt%Li alloy were simulated. The model was validated in terms of mass conservation and kinetics of porosity evolution. The effects of initial hydrogen concentration, initial Li content, and cooling rate on the size, distribution, morphology, and number of pores were quantitatively characterized.

2 Model theory

The focus of this paper is to simulate the hydrogen porosity evolution during the solidification of ternary Al-Cu-Li alloys, which mainly involves phase transformations, including solid, liquid, and gas. The material property data were obtained from thermodynamic calculations. The mesoscopic and microscopic scale simulations of primary dendrites and porosity nucleation and growth have been performed using a combination of the stochastic nucleation model and the cellular automata-finite difference (CA-FD) model. In this model, we just consider hydrogen porosity with an equivalent diameter greater than 15 μm. Therefore, the computational domain consists of a cubic grid with a cell size of 15 μm, and every cell has such information as temperature, solute concentration, hydrogen concentration, and pressure. Previous studies[28-30] have shown that the grid size determines the convergence due to the fast diffusion of hydrogen but the domain size over 1 mm has a negligible impact on the kinetics of hydrogen microporosity evolution. Therefore, a domain size of 1.5 mm×1.5 mm×1.5 mm was chosen in this study.

The superheat from experiments was 96 °C above the liquidus which was used as the average temperature in each cell. Every cell was initially set to the liquid state, and solidification starts from the nucleation stage which follows a Gaussian nucleation function. The growth of the solid is driven by the local undercooling.

2.1.CALPHAD calculations of the Al-Cu-Li alloy system

By minimizing the total Gibbs free energy and solving for the stable phase using the calculation of the phase diagram method (CALPHAD, Pandat, 2021 CompuTherm LLC), the ternary phase diagram and equilibrium solidification path were obtained. Using the physical properties from CALPHAD, the Cellular Automaton Model for Al-Cu-Li alloy was established to simulate the kinetics of porosity nucleation and growth together with the dendritic growth of the primary solid. As shown in Fig. 1 (a), binary Al-4.8wt.%Cu starts solidification from 648 °C and completes at 548 °C, having a solidification range of 100 °C; while the beginning of solidification in binary Al-1.8wt.%Li alloy is from 647 °C and ends at 603 °C, producing a solidification range of 44 °C as shown in Fig.1b. However, when both Cu and Li are added to the Al, the phase diagram varies significantly. The liquidus is reduced by 14 °C and the solidus is lowered by 48 °C compared to the binary Al-Cu phase diagram, producing a long solidification range of 129 °C. In this wide mushy zone, primary Al from 634 °C to 505 °C, which is followed by not only binary eutectic Al_2Cu or Al_3Li phases but also ternary compounds, T1-Al_2CuLi, T2-Al_6CuLi_3, and Tb-Al_7Cu_4Li, as shown in Fig.1c. During the primary Al solidification, the excess solutes (Cu/Li) are rejected to the growing dendrite/liquid interface by partition coefficients of 0.173, and 0.51 for Cu and Li, obtained from Fig. 1 (a) and Fig. 1 (b), respectively. The fraction of eutectics for Al-4.8wt.%-1.8wt.%Li is only 0.11, which has a limited influence on the hydrogen porosity growth due to their fast growth rate. According to previous *in situ* observations [12, 14, 27, 28], porosity nucleated in the liquid at a solid fraction from 0.3~0.6, and the primary α-Al at 0.89 would complete all nucleation stages of porosity. Therefore, we will consider the primary α-Al nucleation and growth and its iterations with hydrogen porosity and ignore the effect of eutectic on porosity in this study.

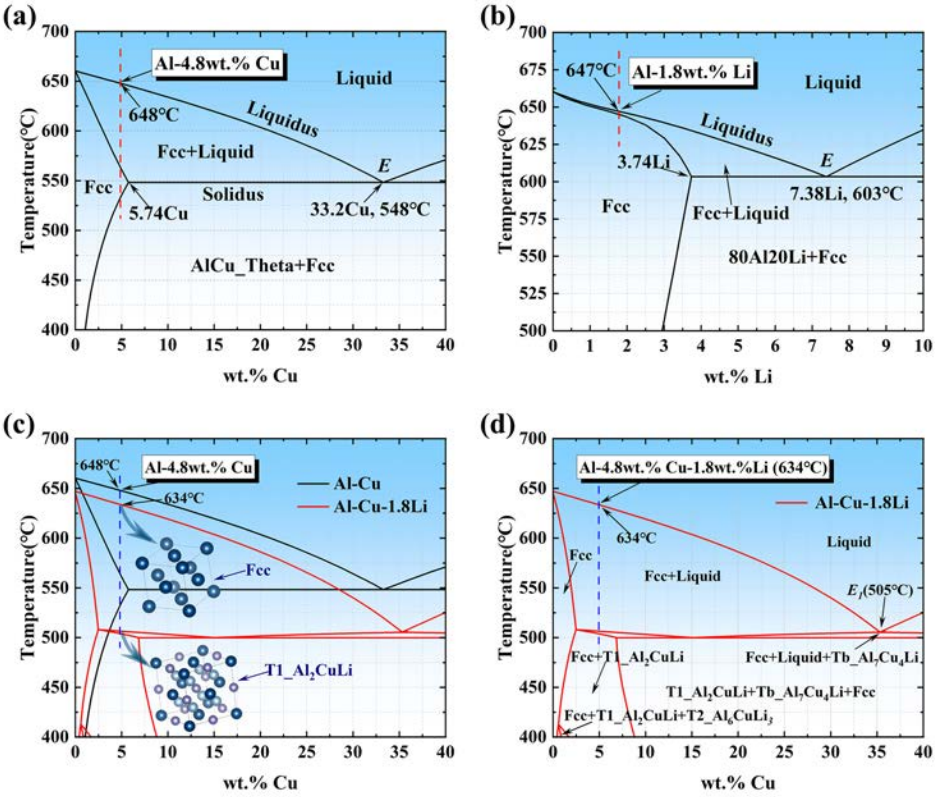

Fig. 1 Binary phase diagrams of Al-rich side: (a) Al-Cu; (b) Al-Li; (c) Al-Cu phase diagram with constant 1.8wt.% Li; (d) labeled phases in the Al-*x*Cu-1.8Li system

As shown in Fig. 2 (a), when the Al-4.8 wt.%Cu-1.8 wt.%Li alloy is cooled from the high-temperature liquid to 634 °C, the primary phase begins to crystallize in the liquid ($L \rightarrow \alpha$-Al) upon a few degrees of undercooling. The primary α-Al dendrites and interdendritic liquids grow into a mushy zone with solid fractions increasing from 0 to 0.89 during this period of solidification. When the temperature is reduced to 505 °C, the dendrite coherency has been well completed and excess solutes have been rejected to the interdendritic liquids or hydrogen gas porosity. Further cooling would like a eutectic phase transformation of those liquid pockets： L → α-Al+T1. In ternary Al-Cu-Li alloy, the eutectic reaction only happens from 505 °C to 500 °C. As the temperature continues to drop, the liquidus valley is reduced to a ternary eutectic point at 500 °C, ending with the eutectic reaction of L → α-Al+T1+Tb. The equilibrium microstructure is α-Al+T1+T2 at room temperature as shown in Fig.2b. Therefore, the main solidification path can be classified into the following stages：

Stage 1 - Formation of primary α-Al dendrites：

$$\text{Liquid} \rightarrow \alpha\text{-Al } (Fcc) \qquad 634\ ^\circ\text{C} \sim 505\ ^\circ\text{C}$$

Stage 2 - Formation of binary eutectic phases (T1_Al_2CuLi):

$$\text{Liquid} \rightarrow \alpha\text{-Al } (Fcc) + \text{T1\_}Al_2CuLi \quad 505\ ^\circ\text{C} \sim 500\ ^\circ\text{C}$$

Stage 3 - Formation of ternary eutectic phases (T1_Al_2CuLi 、Tb_Al_7Cu_4Li):

$$\text{Liquid} \rightarrow \alpha\text{-Al } (Fcc) + \text{T1\_}Al_2CuLi + \text{Tb\_}Al_7Cu_4Li \quad 500\ ^\circ\text{C}$$

In the non-equilibrium solidification, the solidification path is shown in the upper right corner of Fig. 2 (b). When the temperature is reduced to the liquidus temperature at 634 °C, the primary α-Al phase is formed in the liquid within the wider mushy zone (T_{Liq}-T_{eut}=125 °C). The solid phase fraction of the primary α-Al phase reaches 0.89, which is in excellent agreement with the equilibrium solidification. Compared with Al-Cu alloys, the relatively wide solidification mushy zone is more favorable for the nucleation and growth of hydrogen porosities. Subsequently, the binary eutectic reaction $L \rightarrow \alpha$-Al+T1_Al2CuLi occurs at 509 °C, with the reaction temperature slightly higher than the equilibrium binary eutectic transition temperature. As the temperature continues to decrease, a ternary eutectic occurs at 500 °C ($L \rightarrow \alpha$-Al+T1_Al_2CuLi+Tb_Al_7Cu_4Li). Therefore, the CALPHAD calculations provide the kinetic cellular automaton model with basic physical properties for the Al-Cu-Li alloy as listed in Table 1, including liquidus and solidus temperature, and eutectic point temperature.

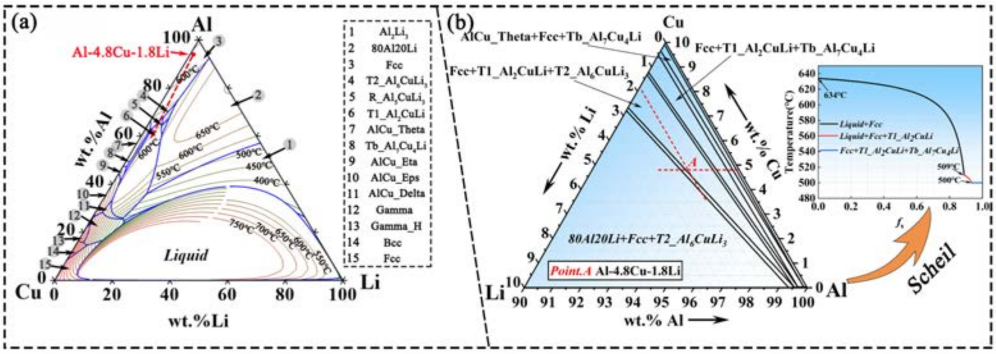

Fig.2 Ternary Al-Cu-Li phase diagram and liquidus projections: (a) liquidus projection; (b) ternary phase diagram with inserts showing non-equilibrium solidification path

2.2.CALPHAD calculations of Hydrogen solubility in Al-Cu-Li

Lithium is a very reactive element that increases the solubility of hydrogen by picking up the hydrogen from the ambient moisture [7, 36]. Studies [6] have shown that Li and H have a strong affinity that increases substantially the hydrogen solubility in Al-Cu-Li alloys, and the LiH crystal structure is shown in Fig. 3. Apparently, hydrogen situates at the interstitial sites of Fcc crystal to form lithium hydride (LiH). Hydrogen is easily dissolved into the Li melts at 287 °C. As shown in the phase diagram, solid lithium hydride forms at low hydrogen pressure and then melted at about 683 °C, so the phase is typically stable during the casting of industrial aluminum-lithium alloys. In this study, we combined the thermodynamic phase boundary data measured by Veleckis *et al*. [31] and the liquidus data obtained from resistivity measurements by Adams *et al*. [32], and the liquidus data acquired by thermal analysis by Messer *et al*. [33], producing a Li-LiH phase diagram at P=1atm as shown in Fig.3.

In the Al-Li liquids, hydrogen accumulation happens right after primary α-Al formation due to the rejection of hydrogen atoms on the advancing solid-liquid interface and/or oxidation impurities [37]. In solid Al-Li, Li tends to bond with H to form LiH [6]. The combination and decomposition of Li and H at the solid-liquid interface is a dynamic process [36]. As the local hydrogen concentration exceeds its supersaturations, hydrogen atoms can assemble into molecules to form hydrogen porosity, which is a complex physicochemical process but highly dependent on hydrogen solubilities. The hydrogen solubility is not only closely related to the temperature but also depends on the Li content. Therefore, we summarized the results of previous studies on the hydrogen solubility of Al-Li alloys and proposed a function for calculating hydrogen solubility suitable for the CA model of Al-Cu-Li alloys.

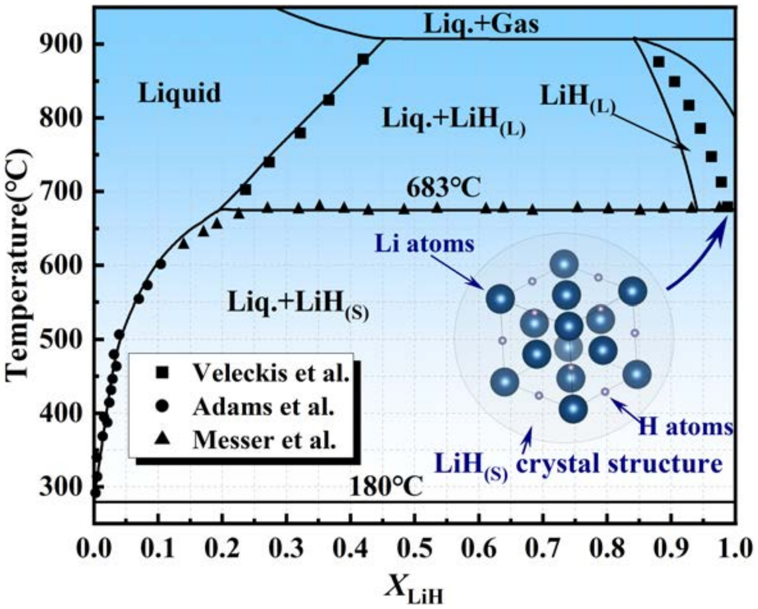

Fig. 3 Calculated Li-LiH phase diagram at P=1atm using reference data [31-33]

As shown in Fig. 4, based on the results of previous studies on the solubility of hydrogen in Al-Cu-Li melts at standard atmospheric pressure, we found that the hydrogen solubility in the liquid obtained from experiments varied significantly under different conditions. The addition of Li to the aluminum alloy greatly increases the solubility of hydrogen in the liquid. In this study, based on the solubility equation obtained by Imabayashi *et al.* [34] and the empirical equation of modified hydrogen solubility summarized by Doutre *et al.* [35], the solubility equation for H in Al-Cu-Li melts is obtained, as shown in Eq. (10). The local hydrogen concentration in the CA model is controlled by the hydrogen solubility. During the simulations, we predict the nucleation and growth of hydrogen porosity using Eq. (10).

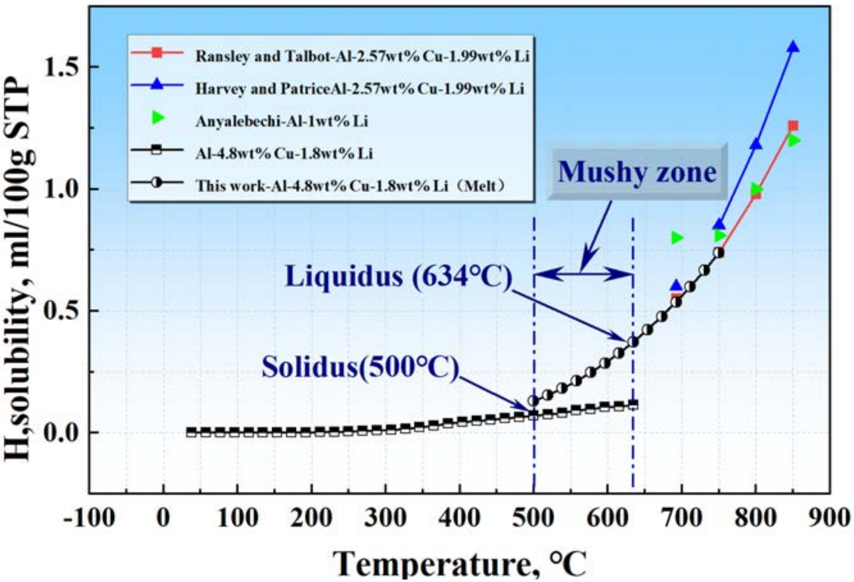

Fig. 4 Summary of previous and calculated data on hydrogen solubilities in Al-Li [6, 7, 36-38]

The detailed assumptions of the model including nucleation and growth of dendrites and hydrogen porosities were given by Lee and other co-investigators [28, 29]. Therefore, only an overview of the model is given below, and details of the new assumptions made and the associated physical equations are written as follows.

2.3.Grain nucleation

For the ternary Al-Cu-Li alloys, the nucleation and growth of the solid are simulated by coupling a cellular automaton (CA) and a finite difference (FD) model. As experimentally observed, heterogeneous nucleation occurs at small undercooling (ΔT). The local undercooling, ΔT_1, is calculated by taking the difference between liquidus temperature and real temperature in the cell at every step [28].

$$\Delta T_1 = T_{\mathrm{eq}} - T_{\mathrm{c}} \tag{1}$$

where T_{eq} is equilibrium liquidus temperature and T_{c} is the local real temperature in every cell. The equilibrium liquidus is given by a linear approximation, as shown below:

$$T_{\mathrm{eq}} = T_{\mathrm{p}} + mC_0 \tag{2}$$

where C_0 is the initial concentration, T_{p} is the melting temperature of pure Al, and the liquidus slope, *m,* can be calculated by:

$$m = \frac{T_{\mathrm{eut}} - T_{\mathrm{eq}}}{C_{\mathrm{eut}} - C_0} \tag{3}$$

where T_{eut} is the eutectic temperature and C_{eut} is the solute concentration at the eutectic point [39]. The distribution of nucleation sites in the domain follows the Gaussian function [17]:

$$\mathrm{P}_n = \frac{1}{\sqrt{2\pi}\Delta T_\sigma} exp\left[-\frac{(\Delta T_n - \Delta T_N)^2}{2(\Delta T_\sigma)^2}\right] \tag{4}$$

where, P_n is the number of nucleation sites, ΔT_n is the actual undercooling in each cell, ΔT_N is the average undercooling required for nucleation, and ΔT_σ is the standard deviation from the Gaussian distribution of the undercooling [39,40].

2.4. Grain growth

The growth of the solid phase in the model follows the principle of continuity and uniformity. At negative temperature gradients, the S/L interface does not stay in a steady state. When there is perturbation at the S/L interface and dendrites will grow into the undercooled melt, due to bigger undercooling in front of the fresh liquid ($dT/dx < 0$), favoring dendritic growth. The growth of dendrites follows the Kurz, Giovanola, and Trivedi (KGT) model [39]. We defined that the growth rate of dendrite tips in the cell is limited by the accumulation of solute at the tip of the growing front. The solute-limited growth from Kurz et al. [39] is used to estimate the tip velocity, where $V_g = \alpha_g \triangle T^2$. The V_g is the growth velocity, $\triangle T$ is the undercooling and α_g is a grain growth rate constant which was set to 7.5×10^{-5} m/s/K^2 for the Al-Cu-Li alloy according to Heard and Gauvin [40, 41]. The expansion of solid phases toward the neighboring cell is controlled by the CA rule, and when the tip of a dendrite in the cell touches the boundary of the neighboring cell, the dendrite will continue to grow in the same direction toward the neighboring empty cell. Therefore, in this model, the cell is not completely filled with the solid before it grows to the next cell. In addition, for the cell at the solid-liquid interface, the solute concentration is partitioned by the equilibrium ratio given by [29]:

$$k_0 = C_s^*/C_l^* \tag{5}$$

where, C_s^* and C_l^* is the equilibrium concentration in the solid and liquid phases, respectively [42].

According to Jackson's α-factor [43], there are half of the atomic sites are empty at the S/L rough interface which can easily bond Al atoms. The growth of dendrites is mainly controlled by the incoming diffusion flux of solute atoms. Due to the rejection of excess solutes at the S/L interface, a concentration gradient at the growing front can be built up which leads to constitutional undercooling. In this research, the growth of the primary α-Al dendrites in a multicomponent Al-Cu-Li system was simulated by combining the CALPHAD and diffusion model. Local solute conservation was established by calculating the equivalent concentration of i_{th} solute in each cell using the following volume-averaged multicomponent diffusion equation [28]:

$$\frac{\partial C_E^i}{\partial t} = \nabla \cdot \left(D_E^i \nabla C_L^i\right) \tag{6}$$

$$C_E^i = f_S C_S^i + (1 - f_S) C_L^i \tag{7}$$

$$D_E^i = f_S D_S^i + (1 - f_S) D_L^i \tag{8}$$

where, C_E^i、$C_L^i$and D_S^i are the equivalent, liquid, and solid concentrations, respectively. D_E^i is the effective diffusion coefficient. In addition, cross-diffusion between all elements is not considered in the simulation. By applying the lever rule, we can obtain the fraction of the primary phase, f_s:

$$\frac{\partial f_S}{\partial t}\left(1 - k_p^i\right) C_L^i = -\nabla \cdot \left(D_E^i \nabla C_L^i\right) + \left[1 - f_S\left(1 - k_p^i\right)\right] \frac{\partial C_L^i}{\partial t} \tag{9}$$

where k_p^i is the partition coefficient of the solute at the solid-liquid interface and f_S is the solid fraction of the primary phase [39].

2.5. Porosity nucleation

Similar to the nucleation of dendrites, the nucleation of the gas porosity in the computational domain follows a stochastic function. When any local hydrogen concentration exceeds its local critical supersaturations, porosity nucleates at this location. The local hydrogen supersaturation is defined by the ratio of the actual hydrogen concentration in the cell to the equilibrium hydrogen concentration, that is, $SS^{H} = C^{\mathrm{H}}/C_{\mathrm{eq}}^{\mathrm{H}}$. Therefore, the nucleation probability of porosity in every cell is controlled by the local hydrogen concentration.

Based on Sievert's law, local hydrogen solubility in Al-Cu-Li alloy melt is described by the following empirical equation [6, 7, 29, 38, 44, 45]:

$$S_1(\mathrm{H}) = \sqrt{\frac{P_{\mathrm{g}}}{P_{\mathrm{atm}}}} 10\left(-\frac{A}{T} + B + C \cdot W_{\mathrm{Cu}} + D \cdot W_{\mathrm{Li}}\right) \tag{10}$$

where P_{g} is the hydrogen porosity internal pressure and P_{atm} (P_{atm}=1atm) is the reference pressure, T is the absolute temperature, and W_{Cu} and W_{Li} are the weight fractions of solutes Cu and Li, respectively. A and B are constants controlled by the equilibrium solubility of hydrogen in pure Al melt, and C and D are the parameters accounting for the effects of dissolved alloying elements Cu and Li on the hydrogen solubility, respectively. In the present work, the constants in Eq. (10) are taken as A=2392 and B=2.256, C=-0.0269, and D=0.027 [43, 44]. In this work, we summarized the previous studies on hydrogen solubility [6, 7, 36-38]. And based on Eq. (10), we derived the hydrogen solubility curve for Al-4.8 wt%Cu-1.8 wt%Li alloy, which is shown in Fig. 4. It shows that the solubility in the liquid is 10 times that in the solid. Depending on different measurements the solubility can vary from 0.01 to 1.58 in Al-Cu-Li system alloys. However, a large reduction of solubility as a result of decreasing temperature is observed. At room temperature, the solubility is only 0.06 ml/100g STP.

2.6. Porosity growth

Once the nucleation barrier is overcome, hydrogen porosity is formed and it maintains the equilibrium concentration which follows the ideal gas law. Its initial radius r_i is controlled by Sieverts' law in combination with the ideal gas equation [47]:

$$r_i = \frac{2\gamma}{\mathrm{P}_a(s^2 - 1)} \tag{11}$$

where γ is the gas-liquid interface energy, P_a is the local pressure. At any position in the calculation domain, as long as the hydrogen concentration reaches its threshold, there will be porosity nucleation. The temperature and hydrogen supersaturation during nucleation are given by the finite difference calculations of diffusion equations.

The growth of hydrogen porosities is controlled by local pressure, hydrogen concentration, and the surrounding environment. If the hydrogen porosity is surrounded by liquid and there is no restriction on its curvature, porosity grows spherically following the ideal gas law, and the radius r_p of the porosity is calculated by the following equation [29]:

$$\frac{4\pi}{3}\left(P_{\mathrm{m}}r_{\mathrm{p}}^{3}+2\gamma r_{\mathrm{p}}^{2}\right)=nRT \tag{12}$$

where P_{m} is the metallostatic pressure, γ is the surface tension as a result of the porosity curvature ($1/r_p$), n is the amount of gas molecular in mole, R is the molar gas constant, and T is the temperature.

Considering the complex morphology of the hydrogen porosities in the interdendritic region during the actual solidification process, for example, the growth of hydrogen porosities is influenced by the surrounding dendrites due to the surface tension. The curvature of the hydrogen porosities gradually deviates from a spherical shape depending on the surrounding solid phases. The radius of curvature of the porosity is determined by the shape of the solid at the contact surface and the interface energy. The relationship between the radius of curvature and solid fraction in the model is as follows [11][48]:

$$r_P=\frac{r_0(1-f_S)}{2\cos\theta},\qquad \cos\theta\neq 0 \tag{13}$$

where r_0 is related to the secondary dendrite arm spacing, and θ is the contact angle between solid-liquid and gas-liquid interfaces [48]. This simulation of hydrogen porosity growth in a dendritic network reproduces the change in volume and morphology of hydrogen porosities growing in narrow channels, due to the influence of the surrounding solid and the increase of gas pressure. The physical parameters of the Al-Cu-Li alloy for simulations are listed in Table 1.

Table 1 Physical constants for CA-FD simulations of the Al-Cu-(Li) alloys

Parameters	**Symbol**	**Al-4.8wt.%Cu**	**Al-4.8 wt.%Cu-1.8 wt.%Li**
Liquidus temperature [TCQ]	T_L	648 °C	634 °C
Solidus temperature [TCQ]	T_S	548 °C	500 °C
Binary, ternary eutectic temperature [TCQ]	T_{eut}	E:548 °C	E_1:505 °C, E_2:500 °C
Al-Cu liquidus slope，α [TCQ]	$m_{L,\alpha}$	-3.5 K/wt.%	
Al-Cu liquidus slope，β [TCQ]	$m_{L,\beta}$	2.67K/wt.%	
Partition coefficient of Cu [TCQ]	k_{Cu}	0.173	
Diffusion coefficient of Cu in liquid [49]	$D_{L,Cu}$	2.4×10^{-9} m^2/s	
Diffusion coefficient of Cu in solid [49]	$D_{S,Cu}$	4.8×10^{-15} m^2/s	
Initial concentration of Cu	$C_{0,Cu}$	4.8 wt.%	
Al-Li liquidus slope，α [TCQ]	$m_{L,\alpha}$	-8.5 K/wt.%	
Al-Li liquidus slope，β [TCQ]	$m_{L,\beta}$	11.5K/wt.%	
Partition coefficient of Li [TCQ]	k_{Li}	0.51	
Diffusion coefficient of Li in liquid [50]	$D_{L,Li}$	4.94×10^{-9} m^2/s	
Diffusion coefficient of Li in solid [50]	$D_{S,Li}$	1.0×10^{-14} m^2/s	
Initial concentration of element Li	$C_{0,Li}$	1.8 wt.%	
Partition coefficient of H [25]	k_H	0.069	
Diffusion coefficient of H in liquid[25, 51]	$D_{L(H)}$	$3.8\times10^{-6}\exp(-2315/T)$ m^2/s	
Diffusion coefficient of H in solid [25, 51]	$D_{S(H)}$	$1.1\times10^{-5}\exp(-4922/T)$ m^2/s	
Initial concentration of H [TCQ]	$C_{0(H)}$	0.25/0.35/0.45 ml/100g STP	
Surface tension at G/L interface [25]	$\lambda_{L/G}$	0.889	
Cell size	$\triangle x$	15 μm	
Time step	$\triangle t$	$(\triangle x^2/D_H)$ s	
Calculation domain 100×100×100	x	1.5mm×1.5mm×1.5mm	

3. Experimental method

The Al-Cu-Li alloy casting experiments were performed by using the vacuum casting technique. To study the effect of the cooling rate on the nucleation and growth of hydrogen porosity, the cooling rate was obtained using finite element calculation in ESI ProCAST. 2018. The 3D Cu mold was chosen with exactly the same geometry as the experiments, with its dimensions shown in Fig. 5b. The casting is 110mm in diameter and 25mm in height. To enhance the accuracy of cooling rate calculation results and reduce the amount of finite element calculation, the mesh size of the casting surface is selected as 1mm and the mesh size of the mold surface is 5mm. The meshes are all triangular and tetrahedral unstructured meshes. The total number of surface mesh is 105240 and the number of volume mesh is 1965430.

To simulate the solidification of the Al-4.8 wt%Cu-1.8 wt%Li alloy in experiments, the mold is filled with liquids at 730 °C, which is cooled by the surrounding copper mold with a heat transfer coefficient (HTC) of 3000W/(m^2·K) [52-54]. The heat is extracted from the mold to the protective Ar gas by natural cooling conditions: HTC=20W/(m^2·K) [55]. The effects of mold pre-heat temperatures ranged from 25 °C, 100 °C, 200 °C, to 300 °C. The temperature-time curves at different mold temperatures were obtained from finite element simulations, and the corresponding average cooling rates at different mold temperatures were calculated according to the ratio of temperature variation from liquidus to solidus over solidification time, $R=\triangle T/\triangle t$, as shown in Fig. 6. The average cooling rates were taken as 8.5 °C/s (mold temperature =25 °C), 7.2 °C/s (100 °C), 5.3 °C/s (200 °C), and 3.6 °C/s (300 °C), respectively. In addition, the experimental results at a mold temperature of 25 °C and a cooling rate of 8.5 °C/s were compared with the CA-FD simulation results for verification. Fig. 5 shows the casting samples and meshes of the mold and cross-section of the mold.

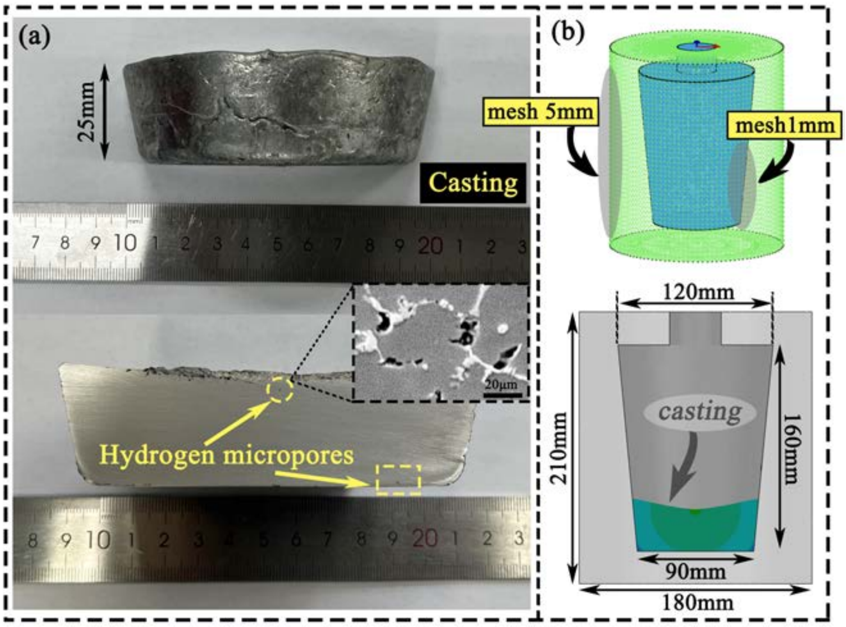

Fig. 5 Samples from experiments and geometry for simulation: (a) images of the as-cast sample and its cross-section; (b) FEM meshes of the copper mold and liquid metal filling

Before the casting started, the raw materials were prepared according to the mass ratio and placed in a graphite crucible. The graphite crucible and raw materials were preheated at 200 °C for 2 hours to remove any moisture in the cavity. Afterward, the melting of the alloy was performed in an Ar gas protective environment at a pressure of 0.5MPa. The heat-up only took 15 minutes to 730 °C using induction and electromagnetic stirring. The holding time was set to 15 minutes before the melt was filled into the copper mold to achieve rapid cooling.

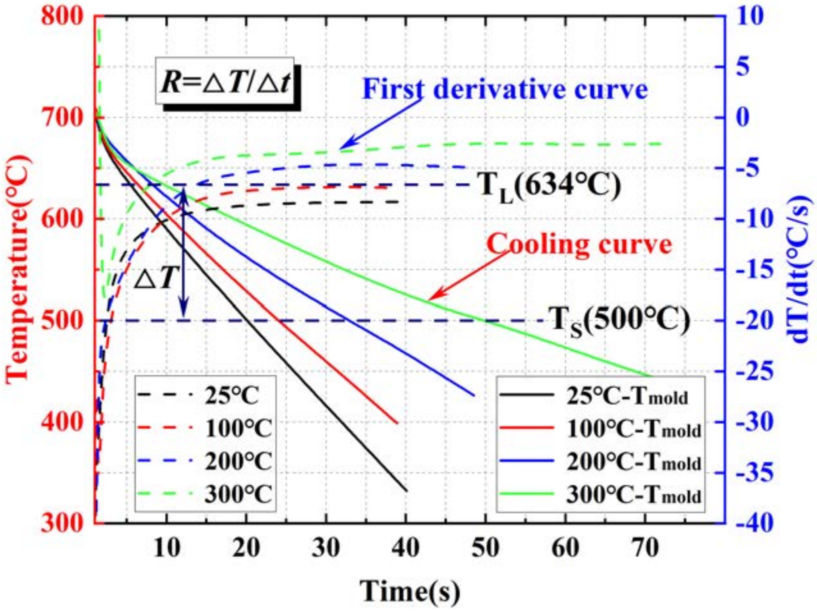

Fig. 6 Temperature and cooling rates from 4 initial mold temperatures: 25, 100, 200, and 300 °C

The initial hydrogen concentration C_H^0 (mL/100 g Al) of the samples was measured using the reduced pressure test (RPT) method, which can be calculated as:

$$C_{\mathrm{H}}^{0} = K_0\left(\frac{1}{D_{rp}} - \frac{1}{D_{th}}\right) \tag{14}$$

where D_{rp} is the density of the reduced pressure sample, D_{th} is theoretical density, and K_0 is the gas law constant which can be further expressed as [45]:

$$K_0 = \frac{P_2}{760} \times \frac{273}{T_2} \times 100 \tag{15}$$

where P_2 is reduced pressure (unit: mm Hg) and T_2 is alloy solidus temperature (unit: K). In the present case, the average measured density was D_{rp}=2.36 g/cm^3 and RPT pressure is P_2=100 mm Hg. Meanwhile, for this experimental alloy, its theoretical density is D_{th}=2.7 g/cm^3 and its solidus temperature is T_2=773 K (500 °C). By plugging these numbers into Eq. (14) and Eq. (15), the hydrogen content can be calculated as C_{H}^{0} = 0.25 mL/100 g Al. In this research, we set up three sets of initial hydrogen concentration gradients (0.25/0.35/0.45 ml/100g) based on the actual Al-4.8 wt%Cu-1.8 wt%Li alloy hydrogen content to quantitatively characterize the effect of initial hydrogen concentration on the evolution of hydrogen porosities.

In addition, to accurately analyze the size, number, and distribution of pore in Al-Cu-Li alloy samples, quantitative 3D characterization of hydrogen porosity was performed in this work using X-ray computed tomography (XCT) on a ZEISS Xradia 520 Versa machine. The fundamental principle of XCT is to obtain a grayscale projection map with structural information based on the attenuation and absorption properties of radiation in the material being examined. Then threshold segmentation is used to separate the porosity with lower grayscale values. In the XCT experiments, the energy level was set to 50kV and 80 μA. The sample size was a 3mm cylinder in diameter (the sampling position is the center of the casting), which is placed within 1mm away from the x-ray source. By fine-tuning the distance of the microscope to the sample, a resolution of 1 μm pixel is achieved. As the sample rotated 360°, a total of 1005 images were collected and then reconstructed to 3D volume data. After reconstruction, the volume data is processed by noise reduction filtering and any artificial imaging defects have been eliminated. A region of interest with a volume of 1.37×10^{9} μm^{3} was obtained for further analysis. The binary thresholding was adopted for the porosity segmentation since the beam hardening has been removed by the reconstruction algorithm. Quantifications of hydrogen porosities over 3.3 μm×3.3 μm×3.3 μm voxels have been successfully achieved by statistical analysis using Avizo (ThermoSientific.2019).

4. Results and discussion

The effects of initial hydrogen concentration, cooling rate, and Li concentration on the size, morphology, and distribution of pores in Al-Cu-Li alloys have been quantified by using X-ray microtomography and compared to simulation results as detailed in the following section.

4.1. Evolution of solid phase, hydrogen concentration, and porosity

The 3-D CA model adopts a computational domain of 100×100×100 cells to simulate the nucleation and growth of hydrogen porosity and its interaction with surrounding dendritic structures during the solidification of Al-Cu-Li alloys, and the simulation parameters are shown in Table 1. Fig. 7 shows the dendrite morphology, hydrogen concentration distribution, and pore evolution for different solid fractions in the solidification of Al-4.8 wt%Cu-1.8 wt%Li alloy. The cooling rate is 8.5 °C/s and the initial hydrogen concentration is 0.25 ml/100g.

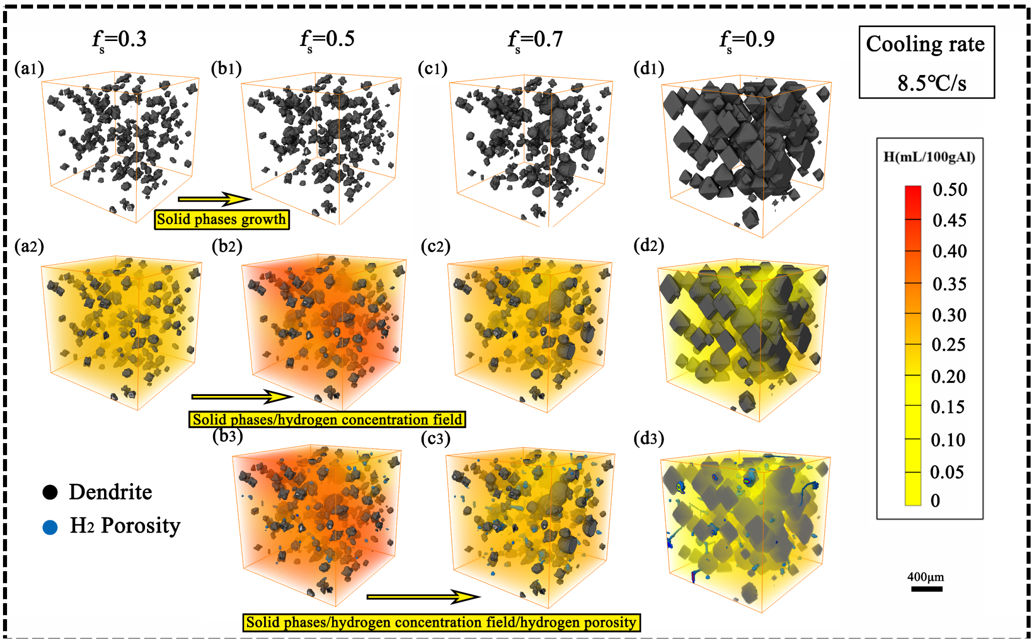

Fig. 7 Hydrogen concentration and porosity morphology at the cooling rates of 8.5 °C/s as a function of solid fractions (f_s): 0.3, 0.5, 0.7, and 0.9

At the beginning of solidification, the solid phase nucleates in such cells that exceeds critical undercooling. As temperature drops, the nuclei started growing into dendrites following the KGT model, and the decentered square algorithm is used to consider the grain anisotropy during growth. The equiaxed dendrite evolution of Al-4.8 wt%Cu-1.8 wt%Li alloy at a cooling rate of 8.5 °C/sis shown in Fig. 7(a1)-7(d1). According to the simulation results, the local maximum hydrogen concentration in the liquid is 0.36 mL/100g when the solid fraction is 0.3 and the temperature is 623 °C. As shown in Fig. 4, the hydrogen solubility in the liquid is 0.34 mL/100g at 623 °C and the maximum local supersaturation of hydrogen (SS^H) is 1.06 according to $SS^H = C^{\mathrm{H}}/C^{\mathrm{H}}_{\mathrm{eq}}$. At this time, there is no hydrogen microporosity nucleation in the liquid, and incubation occurs. With the growth of equiaxed dendrites, more and more hydrogen atoms are partitioned to the S/L interface. When the solid fraction reaches 0.5(608 °C), microporosity nucleation occurs in the interdendritic liquids, and most of the hydrogen porosities showed a spherical shape since they are not limited by the equiaxed dendrites. At this time, the hydrogen solubility in the liquid is 0.31mL/100g. According to the hydrogen concentration distribution in Fig.7 (b2), the maximum hydrogen concentration is 0.47 mL/100g, which gives an SS^H at 1.52 in the liquid exceeding the critical conditions for nucleation. To determine the hydrogen supersaturation required for porosity nucleation, Lee and Hunt *et al.* [11] applied the Lever Rule to calculate the hydrogen concentration in the liquid between dendrites in the local range (f_s<0.5), with the following expression:

$$C_H = \frac{C_o}{1-(1-k)fs} \tag{14}$$

where C_0 is the initial hydrogen concentration, f_s is the fraction solid and k is the partition coefficient of hydrogen between solid and liquid aluminum. When the solid fraction is 0.3, the local hydrogen concentration in the liquid is 0.346 mL/100g, and when the solid fraction is 0.5, the C_H is 0.467 mL/100g, which is very similar to our simulation results. When the solid fraction increased to 0.7 (577 °C), hydrogen porosities grow irregular elongated shapes among the adjacent dendrites, indicating that the growth of hydrogen porosity was restricted by the growing dendrites. The local hydrogen concentration in the liquid was significantly depleted due to the absorption of hydrogen in the growing microporosities compared to the hydrogen levels at f_s=0.5 where the maximum hydrogen concentration is 0.22 mL/100g. In addition, as shown in Fig.7(b3)-7(d3), the hydrogen concentration in the liquid around the porosity is lower than that in other locations, indicating that the growth of the hydrogen porosity absorbs the hydrogen from the surrounding liquid. According to Ding *et al.* [62], hydrogen porosities nucleate and grow when the hydrogen concentration in the mushy zone reaches supersaturation. The growth of hydrogen porosities during solidification can be explained by the following mass absorption rate equation.

$$R_{\mathrm{H}} = \frac{\partial\left[\left(C_{\mathrm{l}}(\rho_{\mathrm{l}} f_1 + \mathrm{k}\rho_{\mathrm{s}} f_{\mathrm{s}})\right)\right]}{\partial t} + \nabla \boldsymbol{j} \tag{15}$$

where R_H is the absorption rate per unit volume of hydrogen porosity, and the first term on the right is the reduction of hydrogen atoms in the melt as it diffuses into the microporosities and incoming flux j of hydrogen from other sources. When the solid fraction increases to 0.9 (501 °C), most of the hydrogen porosities show irregular morphology, only a few of the hydrogen porosities still keep the spherical morphology, and the hydrogen concentration in the liquid is 0.02 mL/100g, lower than that at the solid fraction of 0.3. In summary, as the temperature decreases continuously, the hydrogen concentration in the liquid increases to supersaturated levels. Hydrogen porosity nucleates in the liquid when the nucleation threshold ($SS^H = 1.52$) is reached. Then the hydrogen in the liquid is depleted and diffuses into porosity. When the solid fraction is 0.9, porosity is restricted by the surrounding dendrites and absorbs the hydrogen from the surrounding liquid to form irregular shapes according to Eq.13.

4.2. Effect of initial hydrogen concentration

Lee and Hunt [65] were the first to perform *in situ* observation of porosity formation in Al-Cu and Al-Si binary alloys and studied the influence of hydrogen concentration on porosity growth kinetics. However, In-depth studies on the nucleation and growth of hydrogen porosity at different initial hydrogen concentrations in ternary alloys have not been reported. In particular, when Li is added to the Al-Cu binary alloys, the solidification range extends from 100 °C to 134 °C which gives twice the time for diffusion of hydrogen from liquids to porosity. In the part, based on the hydrogen content in actual Al-Cu-Li melts, we set up three groups of different hydrogen concentrations (0.25/0.35/0.45 ml/100g) for investigating how the initial hydrogen content determines the nucleation and growth of the hydrogen porosities. Fig.8 shows the final morphology, distribution, and volume of hydrogen porosities for three different initial hydrogen concentrations at cooling rates of 3.6 °C/s (Fig. 8 (a), (d), (g)),8.5 °C/s (Fig. 8 (b), (e), (h)) and 15 °C/s (Fig. 8 (c), (f), (i)), respectively. When the initial hydrogen concentration is 0.25ml/100g, pore volume is small and grows independently towards each other as shown in Fig. 8 (a)-8 (c). As the initial hydrogen concentration increases, hydrogen supersaturation reaches the critical value at the early solid fraction. The simulation results show that the hydrogen porosity nucleation temperature is

608 °C and the solid fraction is 0.5 when the initial hydrogen content is 0.25 ml/100g. As the initial hydrogen content increases to 0.45 ml/100g, the porosity nucleation temperature then increases to 612 °C (f_s=0.48), i.e., increasing the initial hydrogen concentration improves the possibility of high-temperature nucleation. Therefore, there will be a long time for the hydrogen porosities to grow in the liquid and eventually recombines into long strips. In addition, the initial hydrogen concentration is raised, increasing the number of hydrogen molecules absorbed by the porosity per unit time, i.e., $P_g > P_m + 2\gamma/r_p$, and the porosity grew rapidly. If the porosity is quantitatively characterized by spherical hydrogen porosity models or equivalent diameters, the results cannot accurately predict the effects of hydrogen concentration on microporosity morphology. In this case, we predict the effect of pore defects by characterizing the maximum length (L_{max}) of the hydrogen porosities as shown in table 2 [48].

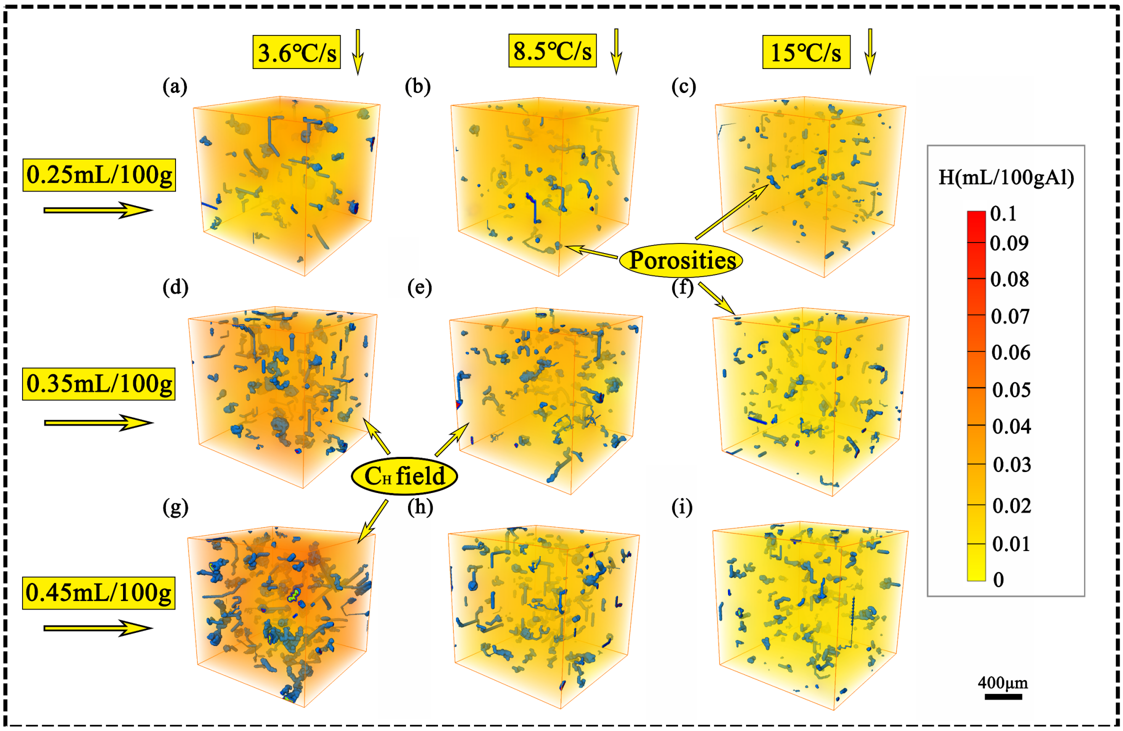

Fig. 8 Simulated pore distribution in the Al-4.8 wt.%Cu-1.8 wt.%Li alloy at different initial hydrogen concentrations: 0.25, 0.35, and 0.45 ml/100g STP

As shown in Fig. 8(g)-8(i), keeping the initial hydrogen concentration constant, the hydrogen concentration in the final liquid is a function of the cooling rates. It is noteworthy that the hydrogen concentrations distributed around the hydrogen porosities are significantly reduced in the liquid, especially in the vicinity of the large hydrogen porosities as shown in Fig. 8 (g). Table 2 shows that when the cooling rates are 15 °C/s

(Solidification time is 8.9s), 8.5 °C/s (15.8s), and 3.6 °C/s (37.2s) respectively, quantitative characterization results of the number, volume, and distribution of hydrogen porosities in Al-4.8 wt.%Cu-1.8 wt.%Li alloys under three different initial hydrogen concentrations. The equivalent diameter (D), geometric length(L), volume percentage($P\%$), density (N_v), and minimum sphericity (S_{min}) are included [29, 48].

Table 2 Quantitative characterization of effects of initial hydrogen concentration on porosity

Cooling rates		D_{avg}	D_{max}	L_{avg}	L_{max}	$P\%$	N_v	S_{min}
0.25 mL/100g	3.6 °C/s	60.2μm	136.0μm	204.8μm	814.8μm	0.35%	19.3mm^{-3}	0.31
	8.5 °C/s	43.1μm	89.4μm	131.4μm	516.5μm	0.18%	30.2mm^{-3}	0.44
	15 °C/s	35.8μm	68.1μm	92.8 μm	362.5μm	0.11%	35.2mm^{-3}	0.52
0.35 mL/100g	3.6 °C/s	55.9μm	120.6μm	187.3μm	606.5μm	0.46%	32.3mm^{-3}	0.36
	8.5 °C/s	50.3μm	110.3μm	151.7μm	520.8μm	0.32%	34.4mm^{-3}	0.40
	15 °C/s	43.1μm	97.1μm	121.0μm	379.7μm	0.22%	40.0mm^{-3}	0.44
0.45 mL/100g	3.6 °C/s	63.1μm	156.4μm	228.0μm	1401.1μm	0.77%	36.4mm^{-3}	0.30
	8.5 °C/s	49.0μm	130.9μm	156.0μm	682.5μm	0.41%	43.9mm^{-3}	0.37
	15 °C/s	47.4μm	89.4μm	132.5μm	581.3μm	0.30%	42.1mm^{-3}	0.46

Taking the characterization results of the cooling rate of 8.5 °C/s (15.8s) as an example, the average equivalent diameter (D_{avg}) of the hydrogen porosities increased from 43.1 μm to 49 μm and the maximum equivalent diameter (D_{max}) increased from 89.4 μm to 130.9 μm with the increase of the initial hydrogen concentration from 0.25 mL/100g to 0.45 mL/100g, an increase of 46%, which is in agreement with the porosity evolution simulation results of Hu *et al.* [44] for Al-Si-Mg alloy and Zhang *et al.* [64] for Al-Si alloy with different initial hydrogen concentrations (0.40 mL/100g and 0.45 mL/100g). In addition, based on previous studies on the effect of the maximum microporosity length on the total fatigue life in the high-cycle fatigue condition, the maximum microporosity length is critical for quantification in the model [48]. As the initial hydrogen concentration increased from 0.25 mL/100g to 0.45 mL/100g, the maximum microporosity length increased from 516.5 μm to 682.5 μm, and the porosity percentage and density also increased by 129% and 45%, respectively. The microporosity sphericity decreases instead, indicating that the increase in initial hydrogen concentration leads to the increase of porosity tortuosity.

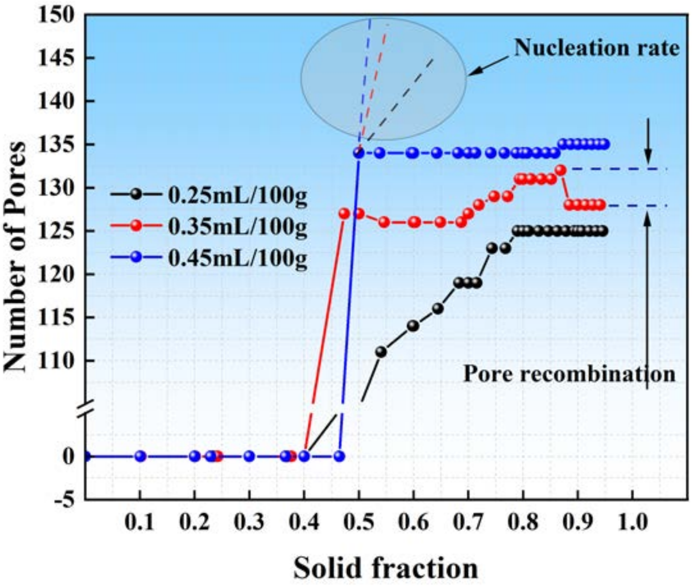

Fig. 9 Relationship between solid fraction and number of porosities with different initial hydrogen concentrations at a cooling rate of 8.5 °C/s

As shown in Fig.9, the number of hydrogen porosities increases from 125 to 135 with the initial hydrogen concentration increasing from 0.25 mL/100g to 0.45 mL/100g during the solidification. The evolution of the hydrogen porosities can be divided into three stages: the initial incubation and nucleation stage, the rapid growth, and the coarsening regime. During the initial incubation and nucleation period($f_s < 0.40$), supersaturation of hydrogen is required for porosity nucleation. As the solidification proceeds, the hydrogen concentration in the liquid rises rapidly, which leads to sufficient supersaturation for the nucleation and growth of hydrogen porosities in the liquid rapidly, and the number of hydrogen porosities increases rapidly at this stage($0.40 < f_s < 0.60$). In the coarsening stage ($f_s > 0.60$), the hydrogen concentration in the liquid decreases, as shown in Fig. 14. The hydrogen in the liquid enters the hydrogen porosities by diffusion and small microporosities shrink accompanying the bigger ones' expansion, driving the pressure inside the hydrogen porosities to follow the ideal gas law. In addition, as shown in Fig.9, the greater the initial hydrogen concentration, the greater the porosity nucleation rate, which shows an increasing slope. The hydrogen supersaturation exceeds the threshold of porosity nucleation, i.e., the nucleation barrier is overcome. The nucleation is instantaneously activated and a large number of porosities are nucleated simultaneously in the liquid among the dendrites. It is noteworthy that with the increasing pore volume, they recombination in the liquid among the dendrites. As shown in Fig.9, when the initial hydrogen concentration is 0.35 mL/100g, the hydrogen porosity recombination, and the number decrease. It can be seen that the recombination between neighboring hydrogen porosities forms a large volume of hydrogen porosities or a "wormhole" between dendrites, as shown in Fig.8d [27,29].

4.3. Effect of cooling rates

The cooling rate plays a critical role in controlling the diffusion time of hydrogen during solidification. As hydrogen diffusion is 1000 times faster than other solutes in the liquid, the excess amount of hydrogen will cluster at different dendrite arm spacing and grain sizes at different cooling rates [27]. Therefore, the cooling rate has a very important effect on the size and quantity of hydrogen porosities [29]. To quantitatively characterize the effects of cooling rate on dendritic growth and porosity evolution during the solidification, different cooling rates were set in the model. Fig.10 shows the distribution, number, and morphology of pores during the solidification of the 3D simulated. The initial hydrogen concentration is 0.25 ml/100g, the pressure is 1atm, and other simulated conditions are kept consistent.

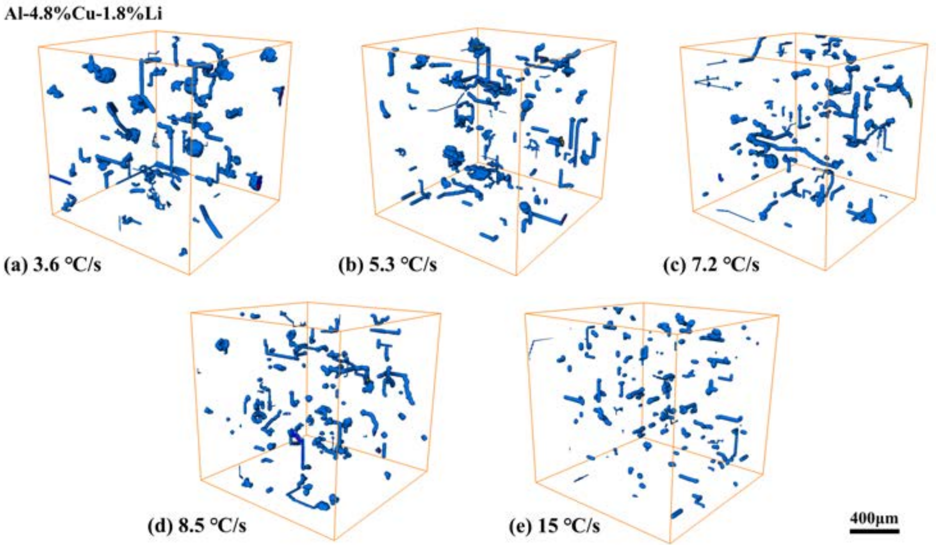

(a) 3.6 °C/s (b) 5.3 °C/s (c) 7.2 °C/s (d) 8.5 °C/s (e) 15 °C/s

Fig. 10 3D porosity distribution in the alloy at the cooling rates of 3.6, 5.3, 7.2, 8.5, and 15 °C/s

Based on a multi-component diffusion model, Wang *et al.* [68] investigated the decrease in porosity density from 5.2 mm^{-3} to 3.5 mm^{-3} when the solidification time was increased from 55s (2.0 °C/s) to 855s (0.2 °C/s) for an Al-Cu-Si ternary alloy ($C_H =$

0.17 ml/100 g). However, the maximum pore size was increased from 2.0 mm to 4.2 mm. As shown in Fig.10, different cooling rates have a significant effect on the hydrogen porosity incubation time and the final number and morphology, and distribution. The size of the hydrogen porosities decreases, and the distribution tends to be uniform as the cooling rate increases from 3.6 °C/s to 15 °C/s. However, the number of hydrogen porosities increases. When the cooling rate is 15 °C/s, the pore density increases to 35.2 mm^{-3} as shown in Table 3. According to Lee and Wang *et al.* [29,68], it was shown that increasing the cooling rate, on the one hand, reduces the solidification time and the time for hydrogen diffusion; on the other hand, the solid formed by rapid cooling limits the growth of hydrogen porosities. Therefore, it is understandable that due to the increase in the cooling rate, the hydrogen atoms rejected by the growing solid front rapidly accumulate at the interface (as a result of the hydrogen solubility reduction in the solid, that is, $k<1$) [28]. The local hydrogen supersaturation increases rapidly due to $SS^{H} = C^{\mathrm{H}}/C_{\mathrm{eq}}^{\mathrm{H}}$ and a large number of porosity nucleation substrates are activated in the liquid, leading to an increase in the number of nucleation and a more uniform distribution. However, The formation of a large number of hydrogen porosities in the early stage consumes hydrogen atoms, resulting in a decrease of hydrogen concentration in the later liquid and insufficient driving force for porosity growth according to the ideal gas law, that is $P_g < P_m + 2\gamma/r_p$. On the contrary, the temperature of the mushy zone decreases slowly at lower cooling rates. Based on the temperature dependence of the diffusion coefficient of hydrogen atoms $D_{L(H)}=3.8\times10^{-6}\exp(-2315/T)$, the thermal movement of hydrogen atoms accelerates and the diffusion rate improves at higher temperatures. As solidification proceeds, $2H_{(\text{in Al-H})} \rightarrow H_{2(\text{gas})}$ transition will occur, and the already nucleated hydrogen porosities are more likely to absorb hydrogen molecules from the surrounding liquid. And the growth of the hydrogen porosities is limited by the surrounding dendrites and is even continuously squeezed, forming irregular morphology eventually.

At high cooling rates, the equiaxed grain structure is refined and the diffusion rate of hydrogen is reduced. In addition, the solubility of hydrogen decreases with decreasing temperature according to Eq. 10. The supersaturation is greater in every site of the mushy zone even though the hydrogen concentration is not equilibrated in the liquid, and this is where nucleation of the hydrogen porosities is more likely. Combined with the limitations of the surrounding fast-growing solid phases, the hydrogen porosities are small in size and high in number compared with low cooling rates, which is consistent with the experimental results obtained by Carlson *et al.*[56]. In summary, the growth of hydrogen porosities is preferentially affected at slower cooling rates, and as the cooling rate increases, the nucleation of hydrogen porosities gradually occupies a dominant position. In the actual casting process, it is necessary to obtain the required microstructure and mechanical properties at a lower cooling rate, such as directional solidification and preparation of single crystals, etc. Attention should be paid to the effect of large-size porosity on the overall performance of the casting.

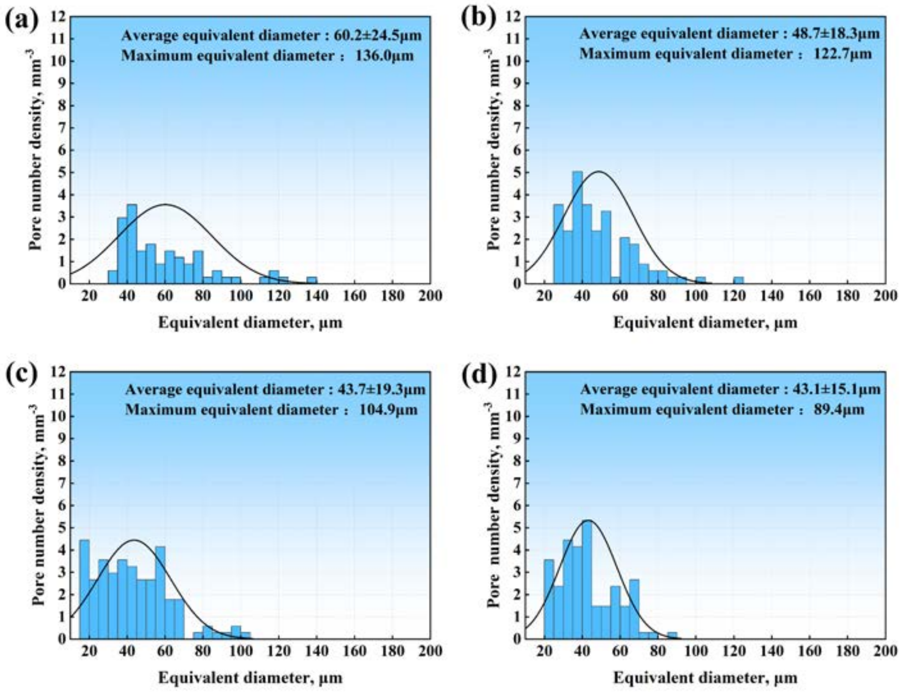

Fig. 11 Statistics of pore sizes at cooling rates of (a) 3.6, (b) 5.3, (c) 7.2, (d) 8.5 °C/s

As shown in Fig. 11, the frequency of distribution of porosity equivalent diameter of Al-4.8 wt.%Cu-1.8 wt.%Li alloy gradually shifts downward in a smaller direction as the cooling rate increases from 3.6 °C/s (solidification time is 37.2s) to 8.5 °C/s (15.8s). The average equivalent diameter of hydrogen porosities gradually decreases from 60.2±24.5 μm to 43.1±15.1 μm, and the maximum equivalent diameter decreases from

136.0 μm to 89.4 μm. Combined with the quantitative characterization results of the number, volume, and distribution of hydrogen porosities for Al-4.8 wt.%Cu-1.8 wt.%Li alloy in Table 3, the hydrogen porosity equivalent diameter, geometric length, and volume percentage show an obvious decreasing trend when the cooling rate increases from 3.6 °C/s to 15 °C/s. At the same time, the hydrogen porosity density and sphericity increase instead. Gu *et al.* [67] used a 3D model to predict the relationship between the volume percentage of porosity and the cooling rate as a function of P (%) $=1.5302R^{-0.875}$ of Al-8.5wt%Si binary alloy with initial hydrogen concentration 0.3 mL/100g. When the cooling rate was 8.5 °C/s, the volume percentage was 0.23%, which was very similar to our predicted results, further verifying the accuracy of the simulation results. The trends shown in Fig. 12 are identical to the results of the XTGS experiments [12,29] and in the experiments of Wang [48]. On the one hand, it shows that the increase in cooling rate leads to the rapid nucleation and continuous growth of dendrites in the liquid. Growing hydrogen porosities are restricted by the solid phases, forming scattered micro-hydrogen porosities. On the other hand, when the cooling rate increases, the local hydrogen concentration in the liquid rapidly reaches the saturation state. A large number of nucleation substrates are activated and the number of hydrogen porosity nucleation increases. The above results show that the cooling rate has a significant effect on the volume of hydrogen porosities, and increasing the cooling rate is beneficial to controlling the formation of larger-volume hydrogen porosities during solidification.

Table 3 Quantitative characterization of porosity size distribution at different cooling rates

Cooling rates	D_{avg}	D_{max}	L_{avg}	L_{max}	*P%*	N_v	S_{min}
3.6 °C/s	60.2±24.5 μm	136.0 μm	204.8 μm	814.8 μm	0.35%	19.3mm^{-3}	0.31
5.3 °C/s	48.7±18.3 μm	122.7 μm	172.4 μm	1007.8 μm	0.25%	27.6mm^{-3}	0.35
7.2 °C/s	43.7±19.3 μm	104.9 μm	145.3 μm	859.3 μm	0.22%	29.1mm^{-3}	0.41
8.5 °C/s	43.1±15.1 μm	89.4 μm	131.4 μm	516.5 μm	0.18%	30.2mm^{-3}	0.44
15 °C/s	35.8±11.0 μm	68.1 μm	92.8 μm	362.5 μm	0.11%	35.2mm^{-3}	0.52

According to the hydrogen porosity growth law proposed by Lee and Atwood [28], the radius of the porosity is limited by the solid phase fraction at the solid-liquid interface, as shown in Eq. 13. And the relationship between the secondary dendrite arm spacing λ_2 and the cooling rate proposed by the Hunt-Lu model [63], it is clear that increasing the cooling rate decreases the λ_2, increases the solid phase fraction per unit time, decreases the $r_o(1-f_s)$ term, and the porosity radius decreases. On the contrary, the porosity size is large and irregular at low cooling rates, which is consistent with the quantitative characterization results, as shown in Fig. 12. In the casting process of alloys with high hydrogen content, the casting quality can be effectively controlled by adjusting the cooling rate [16,48].

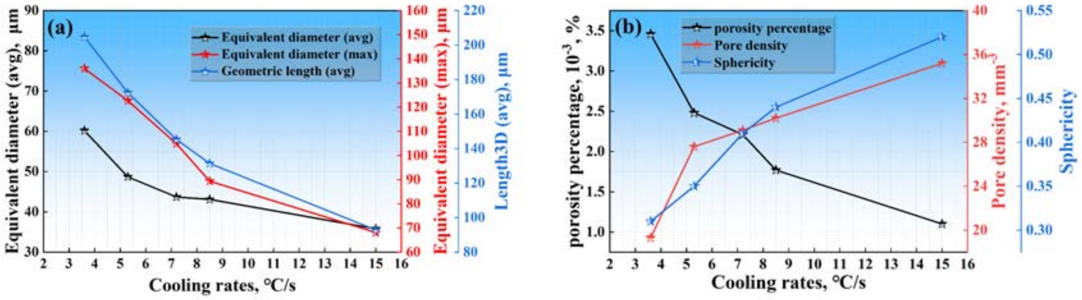

Fig. 12 Hydrogen porosities from simulations in the Al-4.8 wt.%Cu-1.8 wt.%Li alloys: (a) equivalent diameter, geometric length of hydrogen pores; (b) pore number density, volume percentage, sphericity as a function of cooling rates

4.4. Influence of Li element

To investigate the effect of Li on the evolution of hydrogen porosities, two compositions of Al-4.8 wt%Cu and Al-4.8 wt%Cu-1.8 wt%Li alloys were simulated under the same cooling rate and initial hydrogen concentration conditions. The simulated results were compared and analyzed as shown in Fig.13. The addition of 1.8wt% Li significantly increases the average and maximum equivalent diameter, volume percentage, and number density. According to the equilibrium solidification path in Fig. 2, the eutectic phase content increases, and the solidification range widens from 100 °C to 134 °C after the addition of 1.8 wt%Li. And the liquid fraction is 10% at 505 °C, indicating that more liquid persists to a lower temperature compared to the Al-4.8 wt%Cu alloy that has been fully solidified at 548 °C, which is beneficial to the growth of hydrogen porosities in the dendritic liquid.

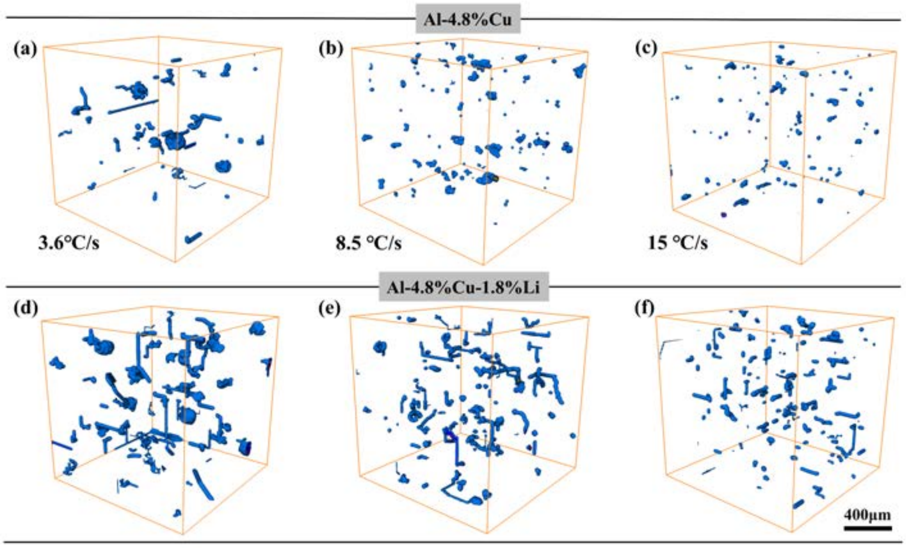

Fig. 13 Comparison of 3D porosity distribution in Al-4.8 wt%Cu and Al-4.8 wt%Cu-1.8 wt%Li at cooling rates of 3.6, 8.5, and 15 °C/s

As shown in Table 4, the effect of Li addition on the hydrogen porosity average (maximum) equivalent diameter, average (maximum) geometric length, volume percentage, density, and sphericity is quantitatively characterized. When the cooling rate is 8.5 °C/s, the average geometric length (L_{avg}) of the porosity increased from 60.1 μm to 131.4 μm and the maximum geometric length (L_{max}) increased from 201.2 μm to 516.5 μm with the addition of 1.8 wt.%Li. The underlying effect of Li on hydrogen porosity nucleation and growth is because of the early nucleation of porosity at the S/L interface due to the increased supersaturations. In addition, at lower temperatures (505 °C), some of the liquid is still present in the Al-4.8wt% Cu-1.8 wt%Li alloys (as compared to Al-4.8 wt%Cu alloys), and the hydrogen porosities can grow freely among dendrites in the liquid. The volume and density of porosity increase, and the morphology evolves irregularly, resulting in a large number of "wormholes" with a wide range of distribution [13]. The appearance of long-strip porosity indicates that the solid and hydrogen porosity grow coordinately during the solidification, which eventually presents the shape of "wormhole". In the actual casting process, this balance can be broken by adding grain refiners, thus reducing the production of long-strip porosity.

Table 4 Quantified effects of Li on the number, volume, and distribution of hydrogen porosities

Cooling rates		***D_{avg}***	***D_{max}***	***L_{avg}***	***L_{max}***	***P%***	***N_v***	***S_{min}***
Al-4.8 wt.%Cu	3.6 °C/s	51.0 μm	106.8 μm	163.6 μm	756.6 μm	0.14%	11.0mm^{-3}	0.42
	8.5 °C/s	32.0 μm	67.6 μm	60.1 μm	201.2 μm	0.09%	29.0mm^{-3}	0.59
	15 °C/s	27.4 μm	58.5 μm	44.7 μm	154.5 μm	0.05%	31.7mm^{-3}	0.69
Al-4.8 wt.%Cu-1.8wt.% Li	3.6 °C/s	60.2 μm	136.0 μm	204.8 μm	814.8 μm	0.35%	19.3mm^{-3}	0.31
	8.5 °C/s	43.1 μm	89.4 μm	131.4 μm	516.5 μm	0.18%	30.2mm^{-3}	0.44
	15 °C/s	35.8 μm	68.1 μm	92.8 μm	362.5 μm	0.11%	35.2mm^{-3}	0.52

The liquidus temperature of the primary phase was reduced from 648 °C to 634 °C after the addition of 1.8 wt.% Li, as shown in Fig.14 (a), (b). The addition of Li increases the incubation period of porosity nucleation. This is consistent with Eq. 10, where the addition of Li decreases the solubility of hydrogen in the liquid, and the supersaturation increases. In addition, the rate of porosity nucleation is significantly increased, as shown in Fig.14 (b). It indicates that the hydrogen supersaturation in the liquid among dendrites instantly reaches the critical value (SS^H =1.52) of nucleation. The number of porosity increased from 101 (without Li) to 121 (with 1.8 wt.%Li). It is noteworthy that the hydrogen concentration in the liquid has a large effect on the nucleation and growth of hydrogen porosities. Firstly, the number of hydrogen porosities increases sharply with the increase of hydrogen concentration. After the nucleation sites consume a large amount of hydrogen, the hydrogen concentration in the liquid starts to decrease, but the number of hydrogen porosities remains stable. It shows that the growth of hydrogen porosities dominates at this stage, and the hydrogen porosities grow further by continuously absorbing hydrogen from the surrounding liquid, resulting in the decrease of hydrogen content in the liquid. The maximum hydrogen concentration threshold is 0.47 mL/100g at f_s=0.5, which is consistent with the results of the hydrogen concentration field distribution in Fig 7.

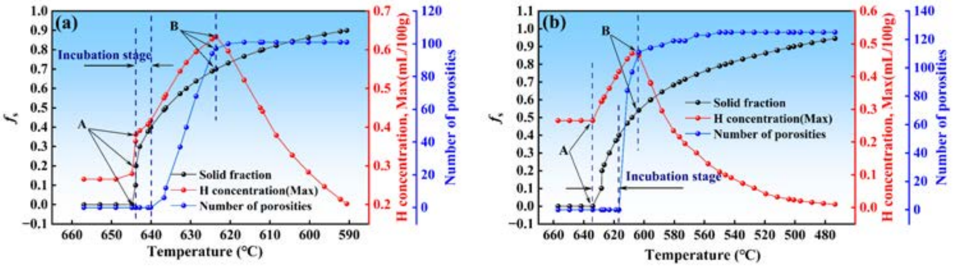

Fig. 14 Solid fraction, hydrogen concentration in liquids, and pore quantity as a function of temperature when cooling at 8.5 °C/s for: (a) Al-4.8 wt.%Cu, (b) Al-4.8 wt.% Cu-1.8 wt.%Li

4.5. Experimental validation

Simulation results were validated by X-ray tomography quantifications. The simulated cooling rate of 8.5 °C/s and an initial hydrogen concentration of 0.25 mL/100g were quantitatively compared to experimental casting results at the same initial conditions. Anson and Gruzleski [66] point out that a complex morphology of porosity may be just a few hydrogen porosities independent of each other under SEM. Fig. 15 (a) shows the 2D morphology of the porosity we obtained. However, the three-dimensional characterization results show that these hydrogen porosities are interconnected with each other, as shown in Fig15 (c). The hydrogen porosities are mainly distributed between dendrites at the grain boundaries to form spherical and irregular shapes, as shown in Fig15 (b).

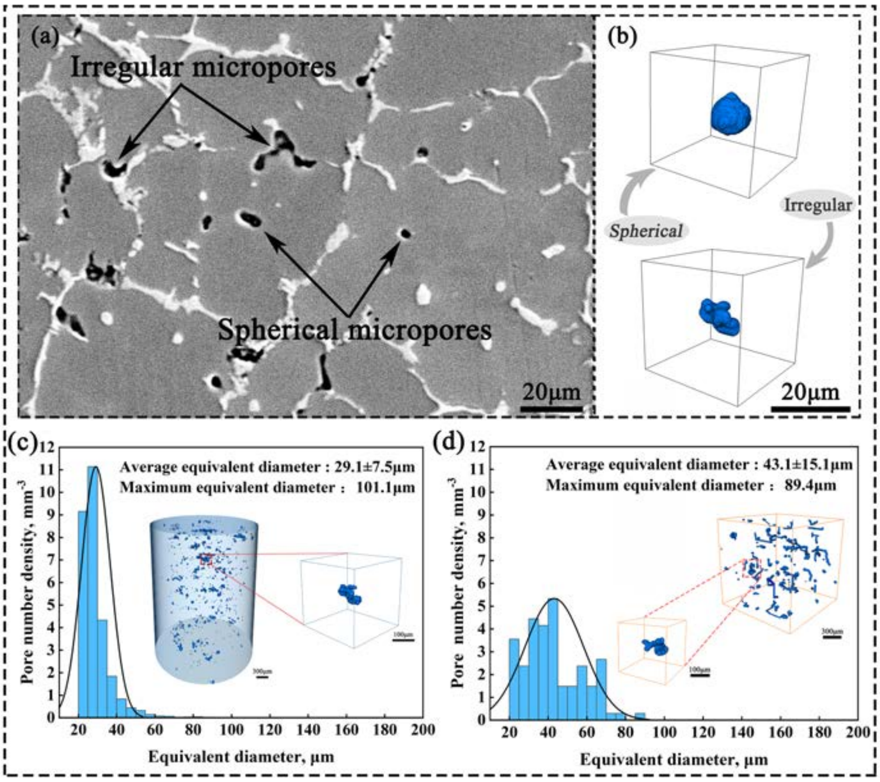

Fig. 15 2D pore morphology from optical metallograph and 3D pore distribution from XCT: (a) Optical metallograph of pore distribution; (b) Extracted two kinds of pore morphology from the same region of the Al-4.8 wt.%Cu-1.8wt.%Li alloy using X-ray computed tomography (XCT); (c) Pore statistical distribution inside the 3.0mm cylindrical sample from the casting; (d) simulated pore statistics and distribution inside a 1.5mm cube using the same cooling rate and initial hydrogen level as experiments

The pore distribution and statistics obtained by XCT characterization are shown in Fig. 15 (c) and compared with the CA-FD predictions (Fig. 15 (c)). The results show that the nucleation and growth of the hydrogen porosities are limited by the surrounding growth of dendrites, eventually taking an irregular shape. The final 3D CA-FD simulation results of the hydrogen porosities agree well with the experimental results by considering the diffusion of hydrogen and the radius of the hydrogen porosities limited by the solid at the interface. Combined with quantitative characterization results, the average equivalent diameter of porosity obtained by the experiment was 29.1±7.5 μm and the maximum equivalent diameter was 101.1 μm, which was extremely similar to the results obtained by simulation. In addition, other experimental results under the same initial conditions were quantitatively compared with the CA-FD simulations, and the results were summarized in Table 5. The porosity information obtained from the experiments and simulations was in good agreement. The 3D CA-FD model could be used to quantitatively predict and visualize the porosity defects in Al-Cu-Li alloys.

Table 5 Comparison of porosity distribution in Al-Cu-Li alloys from simulations and experiments

	D_{avg}	D_{max}	L_{avg}	L_{max}	P%	N_v	S_{min}
Sim.	43.1±15.1 μm	89.4 μm	131.4 μm	516.5 μm	0.18%	30.2mm^{-3}	0.44
Expt.	29.1±7.5 μm	101.1 μm	102.1 μm	591.9 μm	0.54%	38.2mm^{-3}	0.47

4.6. Effect of hydrogen porosities on fatigue life

It has been shown that the presence of hydrogen porosities significantly affects the mechanical properties of the materials, and large porosities are the main initiators for fatigue failures [57-59]. In addition, porosity defects in Al-based alloys often act as the source of crack initiation under stress [57, 60]. The results of the simulation analysis of the average equivalent diameter (D_{avg}) of hydrogen porosities for different cooling rates and hydrogen concentrations are shown in Fig. 16. The analysis is also confirmed previously by Yi and Lee *et al.* [8, 61] for the effect of hydrogen porosities on fatigue life. When the average equivalent diameter is lower than 50 μm (small porosities), the hydrogen porosity defects have no significant effect on the short-cycle fatigue life ($<10^6$ cycles), but can significantly reduce the long-cycle fatigue life ($>10^6$ cycles). When the equivalent diameter is higher than 50 μm (large porosities), the possibility of cracks initiating at the hydrogen porosity defects increases significantly, resulting in a significant decrease in the fatigue life of the experimental specimens at 10^4-10^7 cycles.

The simulation of the average equivalent diameter of hydrogen porosities at different cooling rates and hydrogen concentrations shows that the average equivalent diameter of hydrogen porosities is less than 50 μm when the cooling rate is greater than 5.3 °C/s and the hydrogen concentration is lower than 0.25 mL/100g or the cooling rate is greater than 8.5 °C/s (the hydrogen concentration is in the range of 0.25-0.45 mL/100g), which can effectively improve the fatigue life of the Al-4.8 wt.%Cu-1.8 wt.%Li alloy.

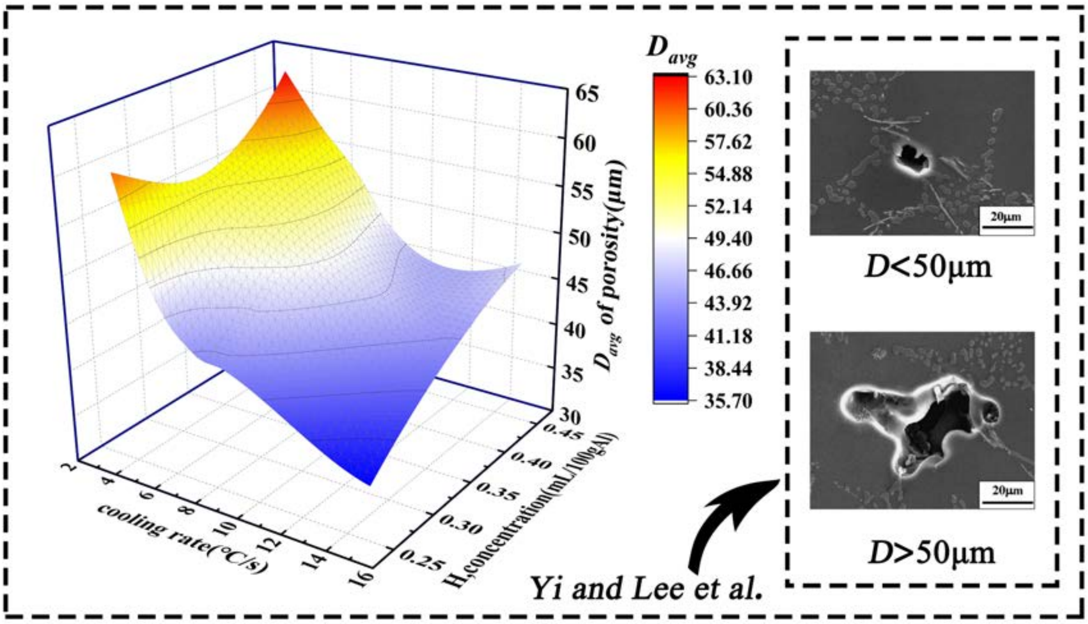

Fig.16 Effect of cooling rate and hydrogen concentration on the average equivalent diameter of porosities and comparison with previous work by Yi and Lee [8, 61]

5 Conclusions

Porosity formation in Al-Cu-Li alloys has been successfully simulated using a multi-component CA-FD model which takes into account the nucleation and growth of dendrites as well as the evolution of hydrogen porosity and its interaction with surrounding dendritic structures. By comparing with experiments, the growth kinetics of porosity are quantitatively obtained and their 3D characteristics have been extracted as a function of solidification time and solute concentration. The major findings from this study are as follows:

The basic mechanism of the effect of initial hydrogen concentration on porosity nucleation and growth is that it increases the supersaturation of hydrogen in the liquid phase and the porosity nucleates at high temperatures. In addition, the increasing number of hydrogen molecules per unit volume could increase the porosity pressure P_g

and lead to the growth of porosity. When the cooling rate was 8.5 °C/s, the average equivalent diameter (D_{avg}) of hydrogen porosities increased from 43.1 μm to 49 μm and the maximum equivalent diameter (D_{max}) increased from 89.4 μm to 130.9 μm with the increase of the initial hydrogen concentration from 0.25 mL/100 g to 0.45 mL/100 g, an increase of 46%. It is worth noting that the initiation and growth of hydrogen porosities are mainly divided into three stages during the solidification: the initial incubation, the nucleation stage, and the subsequent coarsening. This process is accompanied by a significant change in hydrogen concentration in the liquid, which has a "λ" type trend. The number of porosity is stabilized near the maximum value at the equilibrium values of hydrogen concentration.

The basic mechanism of the effect of cooling rate on hydrogen porosity nucleation and growth is the change of solidification time and hydrogen diffusion rate. Increasing the cooling rate reduces the solidification time, decreases the hydrogen diffusion rate, and eventually decreases the volume and increases the number of porosities. The average equivalent diameter (D_{avg}) of the hydrogen porosities gradually decreased from 60.2±24.5 μm to 35.8±11.0 μm and the maximum equivalent diameter (D_{max}) decreased from 136.0 μm to 68.1 μm when the cooling rate increased from 3.6 °C/s to 15 °C/s. Increasing the cooling rate, the shape of porosity tends to be spherical and the number of strip-like "wormholes" is reduced.

The addition of 1.8wt.%Li to Al-Cu alloy leads to the average geometric length (L_{avg}) of the hydrogen porosities increasing from 60.1 μm to 131.4 μm and the maximum geometric length (L_{max}) increasing from 201.2 μm to 516.5 μm. The fundamental reason for the effect of Li on the nucleation and growth of porosity is the early nucleation of porosity at the S/L interface due to the increased supersaturations. At lower temperatures (505 °C), there is still a relatively large amount of liquid present in the Al-4.8 wt%Cu-1.8 wt%Li alloy, and the porosity can grow freely in the interdendritic liquid, increasing the volume and number and distribution ranges.

The accuracy of the simulation results was verified by quantitative characterization of pore size in castings using X-ray tomography. The experimental results proved that the pore volume, number, distribution, and morphology of Al-Cu-Li alloy under the same initial conditions were in good agreement with the simulation results. The validated hydrogen porosity model provides a useful tool for predicting microporosity in Al-Cu-Li alloys.

When the cooling rate is higher than 8.5 °C/s, the average equivalent diameter of microporosities is less than 50 μm, which can effectively improve the fatigue life of the Al-4.8wt% Cu-1.8 wt%Li alloy at 10^6 cycles. If this prediction is accurate, it will have a significant impact on the importance of the control of the Al-Cu-Li alloys process upon fatigue properties.

Acknowledgments

The authors appreciate the public domain cellular automaton code, μMatIC, from Professor Peter D. Lee's group at Imperial College London work. Great support for the X-ray tomography experiments from the Dr. Pengcheng Mao at the Center for Micro and Nano Technologies, Beijing Institute of Technology is sincerely acknowledged. We are also grateful for tremendous helps from all members at the Integrated Computational Materials Engineering (ICME) lab, Beijing Institute of Technology, China. The research work is financially supported by National Natural Science Foundation of China（Project number：52073030）and National Natural Science Foundation of China-Guangxi Joint Fund(U20A20276).

Declaration of Competing Interest

The authors declare that they have no known competing financial interests or personal relationships that could have appeared to influence the work reported in this paper.

References

[1] A. Abd El-Aty, Y. Xu, X. Guo, S.H. Zhang, Y. Ma, D. Chen, Strengthening mechanisms, deformation behavior, and anisotropic mechanical properties of Al-Li alloys: A review, J Adv Res. 10 (2018) 49-67.

[2] A. Chen, Y. Peng, L. Zhang, G. Wu, Y. Li, Microstructural evolution and mechanical properties of cast Al-3Li-1.5Cu-0.2Zr alloy during heat treatment, Mater. Charact.

114 (2016) 234-242.

[3] X. Chen, G. Zhao, G. Liu, L. Sun, L. Chen, C. Zhang, Microstructure evolution and mechanical properties of 2196 Al-Li alloy in hot extrusion process, J. Mater. Process. Tech. 275 (2020) 116348.

[4] B. Decreus, A. Deschamps, P. Donnadieu, J.C. Ehrström, On the role of microstructure in governing fracture behavior of an aluminum–copper–lithium alloy, Mater. Sci. Eng., A 586 (2013) 418-427.

[5] C. Xue, Y. Zhang, P. Mao, C. Liu, Y. Guo, F. Qian, C. Zhang, K. Liu, M. Zhang, S. Tang, J.S. Wang, Improving mechanical properties of wire arc additively manufactured AA2196 Al-Li alloy by controlling solidification defects, Addit. Manuf. 43 (2021).102019

[6] P.N. Anyalebechi, Analysis of the effects of alloying elements on hydrogen solubility in liquid aluminum alloys, Scripta Metallurgica et Materialia 33 (1995) 1209-1216.

[7] P.N. Anyalebechi, Attempt to predict hydrogen solubility limits in liquid multicomponent aluminum alloys, Scripta Mater. 34 (1996) 513-517.

[8] J.Z. Yi, P.D. Lee, T.C. Lindley, T. Fukui, Statistical modeling of microstructure and defect population effects on the fatigue performance of cast A356-T6 automotive components, Mater. Sci. Eng., A 432 (2006) 59-68.

[9] V. Araullo-Peters, B. Gault, F.d. Geuser, A. Deschamps, J.M. Cairney, Microstructural evolution during aging of Al–Cu–Li–x alloys, Acta Mater. 66 (2014) 199-208.

[10] M. Felberbaum, E. Landry-Désy, L. Weber, M. Rappaz, Effective hydrogen diffusion coefficient for solidifying aluminum alloys, Acta Mater. 59 (2011) 2302-2308.

[11] J.D. Hunt, P.D. Lee, Measuring the nucleation of hydrogen porosity during the solidification of aluminum-copper alloys, Scripta Mater. 36 (1997) 399-404.

[12] P.D. Lee, J.S. Wang, R.C. Atwood, Microporosity Formation during the Solidification of Aluminum-Copper Alloys, JOM (J. Occup. Med) 58 (2006) 120-126.

[13] M. Felberbaum, M. Rappaz, Curvature of hydrogen porosities in Al–Cu alloys: An X-ray tomography study, Acta Mater. 59 (2011) 6849-6860.

[14] P.D. Lee, J.D. Hunt, A model of the interaction of porosity and the developing microstructure, Minerals, Metals and Materials Society, Warrendale, PA (United States), 1995.

[15] R.C. Atwood, S. Sridhar, Z. W, P.D. Lee, Diffusion-controlled growth of hydrogen porosities in aluminum-silicon castings: in situ observation and modeling, Acta Mater. 48(2000) 405-417.

[16] J.S. Wang, P.D. Lee, Simulating tortuous 3D morphology of microporosity formed during solidification of Al-Si–Cu alloys, Int. J. Cast. Metal. Res. 20 (2013) 151-158.

[17] J.S Wang, M. Li, J. Allison, P.D. Lee, Multiscale modeling of the influence of Fe content in a Al–Si–Cu alloy on the size distribution of intermetallic phases and hydrogen porosities, J Appl Phys. 107 (2010) 061804-061804-8.

[18] G. Couturier, M. Rappaz, Effect of volatile elements on porosity formation in solidifying alloys, Model. Simul. Mater. Sc. 14 (2006) 253-271.

[19] K. Carlson, S. Ou, R. Hardin, C. Beckermann, Analysis of ASTM X-ray shrinkage rating for steel castings, Int. J. Cast. Metals Res. 14 (2001) 169-183.

[20] K.D. Carlson, Modeling of porosity formation in aluminum alloys, Mater. Sci. Forum. 519-521 (2006) 1699-1706.

[21] K.D. Carlson, Modeling the effect of finite-rate hydrogen diffusion on porosity formation in aluminum alloys, Metall. Mater. Trans. B. 38 (2007) 541-555.

[22] K.D. Carlson, Z.P. Lin, C. Beckermann, G. Mazurkevich, M. Schneider, Modeling of porosity formation in aluminum alloys, Mater. Sci. Forum. 519(2006) 1699-1706.

[23] K.D. Carlson, S.Z. Ou, C. Beckermann, Feeding of high-nickel alloy castings, Metall. Mater. Trans. B 36 (2005) 843-856.

[24] K.D. Carlson, S.Z. Ou, R.A. Hardin, C. Beckermann, Development of new feeding-distance rules using casting simulation: Part I. Methodology, Metall. Mater. Trans. B 33 (2002) 731-740.

[25] M. Zhu, Z. Li, D. An, Q. Zhang, T. Dai, Cellular Automaton Modeling of Microporosity Formation during Solidification of Aluminum Alloys, ISIJ. Int. 54 (2014) 384-391.

[26] A. Zhang, Z. Guo, B. Jiang, J. Du, C. Wang, G. Huang, D. Zhang, F. Liu, S. Xiong, F. Pan, Multiphase and multi-physics modeling of dendrite growth and gas porosity evolution during solidification, Acta Mater. 214 (2021).

[27] Peter D. Lee, J.S. Wang, Modeling of Porosity Formation during Solidification, ASM Int. 22B (2010) 1-11.

[28] R.C. Atwood, P.D. Lee, Simulation of the three-dimensional morphology of solidification porosity in an aluminium–silicon alloy, Acta Mater. 51 (2003) 5447-5466.

[29] J.D. Hunt, P.D. Lee, Hydrogen porosity in directionally solidified aluminium-copper alloys*: A mathematical model*, Acta Mater. 49 (2001) 1383–1398.

[30] P.D. Lee, A. Chirazi, R.C. Atwood, W. Wang, Multiscale modelling of solidification microstructures, including microsegregation and microporosity, in an Al–Si–Cu alloy, Mater. Sci. Eng., A 365 (2004) 57-65.

[31] E. Veleckis, and M. Blander, Lithium-lithium hydride system, J. Phys. Chem. 78 (1974) 1933–40.

[32] M.G.D. P.F. Adams, P. Hubberstey, and R.J. Pulham, Solubilities, and solution and solvation enthalpies, for nitrogen and hydrogen in liquid lithium, J. Less-Common Met. 42 (1975) 325–34.

[33] C.E. Messer, P.C. Maybury, J. Mellor, and R.A. Seales, Solid–Liquid Equilibrium in the Lithium Lithium Hydride System, J. Phys. Chem. 62 (1958) 220-22.

[34] M. Imabayashi, and Y. Sasajima, Solubility of hydrogen in molten aluminum, Keikinzoku 45 (1995) 278-283.

[35] D. Doutre, Internal report, Alcan Int, Ltd, 1991.

[36] J.P. Harvey, P. Chartrand, Modeling the Hydrogen Solubility in Liquid Aluminum Alloys, Metall. Mater. Trans. B 41 (2010) 908-924.

[37] H.M. Lin R Y The Solubility of Hydrogen in Molten Aluminum Alloys, Metall. Trans. A 20 (1989) 1785-1791.

[38] C.E. Ransley, D. Talbot, Wasserstoff-Porositat in Metallen unter Besonderer Berucksichtigung des Aluminiums und Seiner Legierungen, Int. J. Mater. Res. 46 (1955) 328-337.

[39] W. Kurz, B. Giovanola, R. Trivedi, Theory of microstructural development during rapid solidification, Acta metall. 34 (1986) 823-830.

[40] D. W. Heard, R. Gauvin, M. Brochu, Non-equilibrium solute partitioning in a laser re-melted Al–Li–Cu alloy, Acta Mater. 61(2013) 7432-7436.

[41] D. W. Heard, J. Boselli, R. Rioja, E. A. Marquis, R. Gauvin, and M. Brochu, Interfacial morphology development and solute trapping behavior during rapid solidification of an Al–Li–Cu alloy, Acta Mater. 61(2013) 1571-1580.

[42] B. Wang, M. Zhang, J. Wang, Quantifying the effects of cooling rates and alloying additions on the microporosity formation in Al alloys, Mater. Today Commun. 28 (2021).

[43] K.A. Jackson, Crystal growth kinetics, Mater. Sci. Eng. 65 (1984) 7-13.

[44] M. Hu, T. Wang, H. Fang, M. Zhu, Modeling of gas porosity and microstructure formation during dendritic and eutectic solidification of ternary Al-Si-Mg alloys, J. Mater. Sci. Technol. 76 (2021) 76-85.

[45] P.N. Anyalebechi, D.E.J. Talbot, D.A. Granger, The solubility of hydrogen in solid binary aluminum-lithium alloys, Metall. Mater. Trans. B 20 (1989) 523-533.

[46] C. Ho, C. J. Wen, B. A. Boukamp, I. D. Raistrick, W. Weppner, and R. A. Huggins, Use of electrochemical methods to determine chemical-diffusion coefficients in alloys: application to 'LiAI', International Metals Reviews 5(1981).

[47] R.C. Atwood, P.D. Lee, A combined cellular automata and diffusion model for the prediction of porosity formation during solidification, Imperial College London (2000).

[48] J.S. Wang, *In-situ* Observation and Mathematical Modelling of the Nucleation and Growth of Intermetallics and Hydrogen porosities During the Solidification of Aluminium Alloys, Imperial College London (2009).

[49] I.L. Ferreira, J.F. Lins, D.J. Moutinho, L.G. Gomes, A. Garcia, Numerical and experimental investigation of microporosity formation in a ternary Al–Cu–Si alloy,

J. Alloy. Compd. 503 (2010) 31-39.

[50] Q. Chen, L. Zhang, S. Tang, C. Liang, Y. Ma, W. Liu, Examination of dendritic growth and microsegregation during solidification of Al–Li binary alloy using the phase-field simulation coupling CALPHAD data, Calphad 74 (2021).

[51] K.-D. Li, E. Chang, Mechanism of nucleation and growth of hydrogen porosity in solidifying A356 aluminum alloy: an analytical solution, Acta Mater. 52 (2004) 219-231.

[52] C.P. Hallam, W.D. Griffiths, A Model of the Interfacial Heat-Transfer Coefficient for the Aluminum Gravity Die-Casting Process, Metall. Mater. Trans. B 35 (2004) 721-733.

[53] R. Rajaraman, R. Velraj, Comparison of interfacial heat transfer coefficient estimated by two different techniques during solidification of cylindrical aluminum alloy casting, Heat Mass Tran. 44(2008) 1025-1034.

[54] M.L. Xin, Z.D. Wang, B. Lu, Y. Li, Effects of different process parameters on microstructure evolution and mechanical properties of 2060 Al-Li alloy during vacuum centrifugal casting, J. Mater. Res. Tech. 21 (2022) 54-68.

[55] R. Li, Casting process simulation ProCAST from introduction to mastery, Beijing: China Water Conservancy and Hydropower Publishing House (2010).

[56] K.D. Carlson, Z. Lin, C. Beckermann, Modeling the Effect of Finite-Rate Hydrogen Diffusion on Porosity Formation in Aluminum Alloys, Metall. Mater. Trans. B 38 (2007) 541-555.

[57] E. Cakmak, M.N. Gussev, T.R. Watkins, D.J. Arregui-Mena, K.A. Terrani, In-situ x-ray computed tomography analysis of fracture mechanisms in ultrasonic additively manufactured Al-6061 alloy, Addit Manuf. 48 (2021).

[58] Y. Zhang, E. Lordan, K. Dou, S. Wang, Z. Fan, Influence of porosity characteristics on the variability in mechanical properties of high pressure die casting (HPDC) AlSi7MgMn alloys, J Manuf Process 56 (2020) 500-509.

[59] H. Su, H. Toda, R. Masunaga, K. Shimizu, H. Gao, K. Sasaki, M.S. Bhuiyan, K. Uesugi, A. Takeuchi, Y. Watanabe, Influence of hydrogen on strain localization and fracture behavior in Al Zn Mg Cu aluminum alloys, Acta Mater. 159 (2018)

332-343.

[60] D. Chen, X. Zhan, T. Liu, Y. Zhao, N. Qi, L. Sun, Effect of porosity morphology and elements characteristics on mechanical property in T-joints during dual laser-beam bilateral synchronous welding of 2060/2099 Al-Li alloys, Opt Laser Technol. 140 (2021).

[61] Q.G. Wang, D. Apelian, D.A. Lados, Fatigue behavior of A356-T6 aluminum cast alloys. Part I. Effect of casting defects, Journal of Light Metals 1 (2001) 73-84.

[62] Z.Y. Ding, Q.D. Hu, W.Q. Lu, X. Ge, S. Cao, S.Y. Sun, T.X. Yang, M.X. Xia, J.G. Li, In-situ study on hydrogen bubble evolution in the liquid Al/solid Ni interconnection by synchrotron radiation X-ray radiographg, J Mater Sci Technol. 35 (2019) 1388-1392.

[63] J.D. Hunt, S.Z. Lu, Numerical modeling of cellular/dendritic array growth: spacing and structure predictions, Metall Mater Trans. A 27 (1996) 611-623.

[64] Q.Y. Zhang, T.T. Wang, Z.J. Yao, M.F. Zhu, Modeling of hydrogen porosity formation during solidification of dendrites and irregular eutectics in Al-Si alloys, Mater. 4(2018) 211-220.

[65] P.D. Lee, J.D. Hunt, Hydrogen porosity in directionally solidified aluminium-copper alloys: In situ observation, Acta Mater. 45(1997) 4155-4169.

[66] J.P. Anson, J.E. Gruzleski, The quantitative discrimination between shrinkage and gas microporosity in cast aluminum alloys using spatial data analysis, Mater Charact. 43(1999) 319-335.

[67] C. Gu, C.D. Ridgeway, C. Emre, Y. Lu, A.A. Luo, predicting gas and shrinkage porosity in solidification microstructure: A coupled three-dimensional cellular automaton model, J Mater Sci Technol. 49(2020) 91-105.

[68] J.S. Wang, P.D. Lee, Simulating tortuous 3D morphlolgy of microporosity formed during solidification of Al-Si-Cu alloys, Int J Cast Metal Res. 20(2007) 151-158.